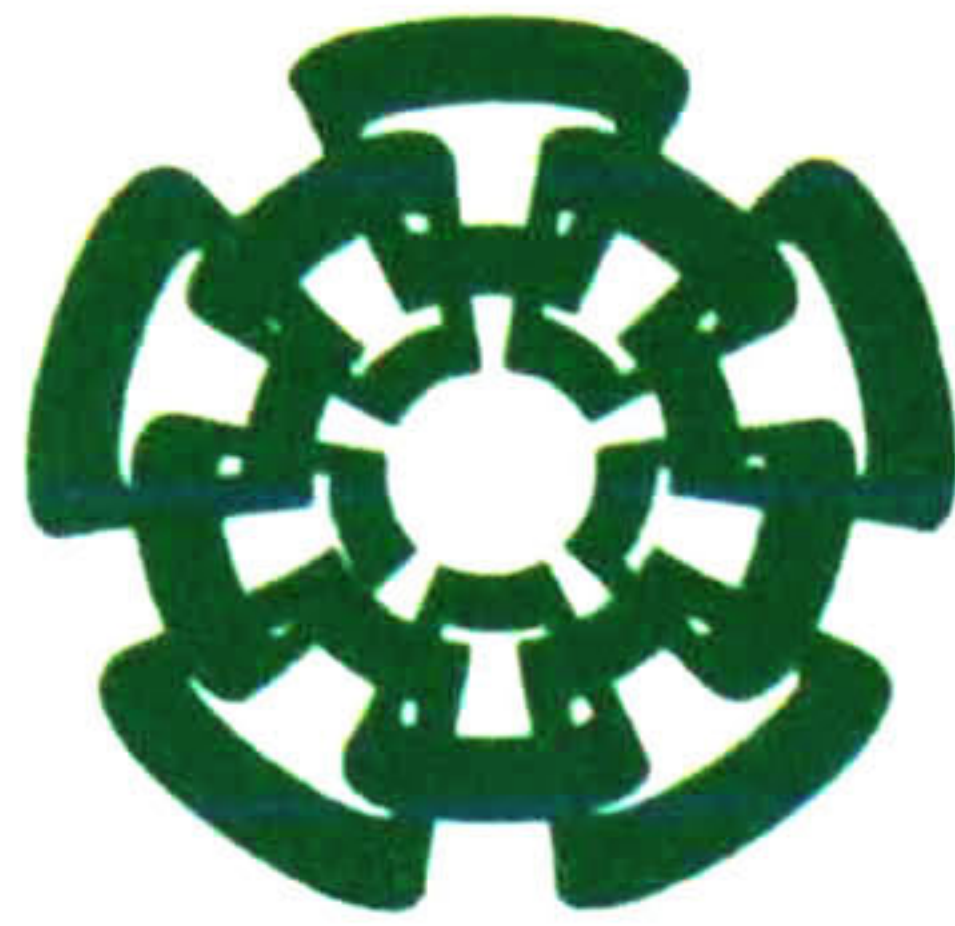


CT-925-251

Nov. 2016

cm /



Centro de Investigación y de Estudios Avanzados
del Instituto Politécnico Nacional
Unidad Guadalajara

**Modelado del Generador Eólico con
Máquina de Inducción Doblemente
Alimentada en el Dominio Armónico
Extendido**

Tesis que presenta:
Uriel Vargas Gazcón

para obtener el grado de:
Maestro en Ciencias

en la especialidad de:
Ingeniería Eléctrica

Director de Tesis:
Dr. Amner Israel Ramírez Vázquez

**CINVESTAV
IPN
ADQUISICION
LIBROS**

CINVESTAV del IPN Unidad Guadalajara, Guadalajara, Jalisco, Agosto de 2015.

CLASIF..	CT00876
ADQUIS..	CT-925-SS1
FECHA:	25-04-2016
PROCED..	DON: 2016
	§



Centro de Investigación y de Estudios Avanzados
del Instituto Politécnico Nacional
Unidad Guadalajara

Extended Harmonic Domain Modeling of a Wind Turbine with Doubly Fed Induction Generator

A thesis presented by
Uriel Vargas Gazcón

to obtain the degree of:
Master of Science

in the subject of:
Electrical Engineering

Thesis Advisor:
Dr. Amner Israel Ramírez Vázquez

Modelado del Generador Eólico con Máquina de Inducción Doblemente Alimentada en el Dominio Armónico Extendido

**Tesis de Maestría en Ciencias
Ingeniería Eléctrica**

Por:

Uriel Vargas Gazcón

Ingeniero en Mecatrónica

Instituto Politécnico Nacional 2008-2013

Becario de CONACYT, expediente no. 300785

Director de Tesis:

Dr. Amner Israel Ramírez Vázquez

CINVESTAV del IPN Unidad Guadalajara, Agosto de 2015.

Extended Harmonic Domain Modeling of a Wind Turbine with Doubly Fed Induction Generator

**Master of Science Thesis
In Electrical Engineering**

By:

Uriel Vargas Gazcón

Engineer in Mechatronics

Instituto Politécnico Nacional 2008-2013

Scholarship granted by CONACYT, No. 300785

Thesis Advisor:

Dr. Amner Israel Ramírez Vázquez

CINVESTAV del IPN Unidad Guadalajara, August 2015.

A mis Padres

Como un testimonio de gratitud y eterno reconocimiento, por el apoyo que siempre se me ha brindado y con el cual he logrado terminar mi Maestría, siendo para mí, la mejor de las herencias.

Con admiración y respeto,
Uriel

ACKNOWLEDGMENTS

I would like to thank my Parents, Soledad and Fausto, for their support and unwavering love. They were always there cheering me up and stood by me through the good and bad times.

To my brothers and sisters, Mitzy, Benjamín, Omar, Luis, and Beatriz, for their friendship, invaluable support, and humor over years.

To my nephews, Dante and Uziel, for bringing me so much happiness.

To my always friend Odette, for all the good time we shared together.

I would also like to express my sincere gratitude to my advisor, Dr. Abner Ramírez, for his excellent guidance, patience, motivation, and immense knowledge. My research and thesis would not have been possible without his help.

To my professors at CINVESTAV, for their contribution to my vocational training.

To my friends at CINVESTAV, for the great moments and experiences lived together; as well as to my friends at Mexico City Metropolitan Area, for their support no matter the distance.

To CINVESTAV, for being an excellent institution, providing me the opportunity to study a Master.

Finally, to CONACYT, for the provided economic support which made my stay easier.

INDEX

Acknowledgments	i
Index	ii
List of figures	iv
List of tables	v
Resumen	vi
Abstract	vii

1 INTRODUCTION

1.1 Role of renewable energies in reducing greenhouse emissions.....	1
1.2 Salient data of wind power around the world	1
1.2.1 Wind power generation in Mexico	2
1.3 WTG systems and power quality	3
1.4 Existent research on WTG with and without harmonics	3
1.5 Problem statement	4

2 MODELING HARMONICS IN POWER SYSTEMS

2.1 Fourier series	5
2.2 Harmonic domain (HD).....	6
2.2.1 Convolution in the HD	8
2.2.2 Linear elements in HD.....	9
2.2.3 Switching function in HD.....	9
2.2.4 Steady-state solution via HD	9
2.2.5 Example	10
2.3 Extended harmonic domain (EHD)	13
2.3.1 Example	14
2.4 Conclusions.....	16

3 WTG EHD MODEL

3.1	General description	17
3.2	DFIG EHD model	17
3.3	Aerodynamic EHD model	21
3.4	Torsional shaft EHD model	22
3.4.1	Mechanical modes	23
3.5	BTB and <i>RL</i> Filter EHD models	23
3.5.1	PWM scheme	24
3.6	AC grid EHD model	26
3.7	Assembling the EHD models	27
3.7.1	Electrical subsystem	27
3.7.2	Mechanical subsystem	30
3.8	Control scheme	30
3.8.1	Low-level control	31
3.8.2	High-level control	33
3.9	High-impact harmonics	36
3.10	WTG system solution	36
3.11	Conclusions	38

4 CASE STUDY

4.1	System description and data	39
4.2	Numerical results	41
4.3	Conclusions	47

5 CONCLUSIONS

5.1	Conclusions	48
5.2	Future work	48
5.3	Publications	49

References	50
-------------------------	-----------

Appendix	52
-----------------------	-----------

LIST OF FIGURES

Fig. 2.1. Example of converting a TD signal into the HD.....	8
Fig. 2.2. Boost converter representation.....	11
Fig. 2.3. Example of switching function.	11
Fig. 2.4. Simulation results a) Current across inductor b) Voltage at capacitor terminals..	12
Fig. 2.5. Simulation results a) Voltage at capacitor terminals b) Current across inductor c) Harmonic evolution of v_c d) Harmonic evolution of i_L	15
Fig. 3.1. Schematic representation of the WTG system.	17
Fig. 3.2. Aerodynamic representation - PSCAD/EMTDC block.	22
Fig. 3.3. Aerodynamic and two-mass representations.....	23
Fig. 3.4. BTB and RL Filter representation.	23
Fig. 3.5. Three-phase converter. a) Control and triangular signals. b) PWM scheme. c) Switching function spectrum.....	25
Fig. 3.6. AC grid connected to the DFIG and BTB converter.....	26
Fig. 3.7. Operation regions of the WTG.....	31
Fig. 3.8. Control scheme of the WTG system.	31
Fig. 3.9. Block diagrams of the RSC control loop.	32
Fig. 3.10. Block diagram of the GSC control loop.....	33
Fig. 3.11. Block diagram of the pitch control.....	34
Fig. 3.12. Power with MPPT process.	35
Fig. 3.13. Flowchart of MPPT.....	35
Fig. 3.14. High-impact harmonics in switching function spectrum.	36
Fig. 4.1. Simulation results a) Wind speed b) Rotor speed c) Pitch angle.	41
Fig. 4.2. Simulation results a) Turbine mechanical torque b) Electromagnetic torque c) Mechanical power from the turbine.	42
Fig. 4.3. Simulation results a) Stator current b) Stator current at fundamental frequency c) “High-impact” harmonics evolution in stator currents.	43
Fig. 4.4. Simulation results a) Rotor current (referred to stator) b) Rotor current at fundamental frequency (referred to stator) c) “High-impact” harmonics evolution in rotor currents (referred to stator).....	44
Fig. 4.5. Simulation results a) THD in stator current b) THD in rotor current (referred to stator).....	45
Fig. 4.6. Simulation results a) Active power from the stator b) Reactive power from the stator.	46

LIST OF TABLES

Table 1.1. Wind power statistics of the IEA member countries, 2013.....	2
Table 2.1. Element representations in TD and HD.....	10
Table 2.2. Parameters of the BC simulation.....	13
Table 2.3. Simulation data of the BC simulation.	14
Table 4.1. System data.....	39
Table 4.2. Simulation data of the case study.	46

RESUMEN

Esta tesis presenta el modelo del generador eólico en el dominio armónico extendido (EHD, por sus siglas en Inglés) basado en el generador de inducción doblemente alimentado (DFIG, por sus siglas en Inglés). La topología del sistema de generación eólico propuesto incluye los siguientes modelos: i) aerodinámico, el cual representa la extracción de energía de la turbina, ii) eje de transmisión, representado por un modelo dos masas, iii) DFIG, iv) convertidor bidireccional, también conocido como “back-to-back” (BTB, por sus siglas en Inglés), v) red de corriente alterna, y vi) filtro pasivo RL .

En esta tesis, el convertidor BTB es representado en el EHD mediante funciones de switcheo que incluyen su correspondiente contenido armónico; esto permite monitorear paso a paso la variación con el tiempo de los armónicos. También permite, entre otras aplicaciones, detectar escenarios de contingencia causados por armónicos específicos. Además, el desempeño del control puede ser mejorado mediante índices de calidad de energía que son proporcionados en forma instantánea por el modelo propuesto.

El modelo propuesto implica mayores dimensiones que su correspondiente representación en el dominio del tiempo el cual está dado por su correspondiente grupo de ecuaciones diferenciales ordinarias (ODEs, por sus siglas en inglés). No obstante, un eficiente remedio es propuesto en esta tesis, el cual consiste en considerar sólo los armónicos más significativos, basado en el espectro frecuencial de la función de switcheo. Esta consideración permite una simulación más rápida para el modelo propuesto.

El modelo del generador eólico en el EHD es validado con el software PSCAD/EMTDC mediante simulaciones. Las principales aplicaciones del modelo propuesto involucran sistemas de conversión de la energía del viento (WECS, por sus siglas en inglés) dentro de las áreas de calidad de la energía y de generación distribuida.

ABSTRACT

This thesis presents an extended harmonic domain (EHD) model of a wind turbine generator (WTG) system based on doubly-fed induction generator (DFIG). The topology of the WTG EHD system includes the following models: i) aerodynamic, which represents the power extraction of the rotor, ii) torsional shaft, represented by a two-mass model of the drive train, iii) DFIG, iv) back-to-back (BTB) converter, v) AC grid, and vi) RL filter.

In this thesis, the BTB converter is represented in the EHD via switching functions that include its corresponding harmonic content; this allows to monitoring step-by-step the harmonics time-variation. Also, it permits, among other applications, to detect contingency scenarios caused by specific harmonics. Moreover, control performance can be improved by means of the power quality indices which are instantaneously available by the proposed EHD model.

The proposed EHD model implies dimensions larger than their corresponding instantaneous variable representations, given by corresponding sets of ODEs. Nevertheless, an efficient heuristic remedy is proposed in this thesis which consists on accounting for “high-impact” harmonics only, based on the converter’s frequency spectrum. This remedy provides a faster simulation by the EHD model.

The proposed model is validated with the PSCAD/EMTDC software tool via simulations. The main applications of the proposed model are in wind energy conversion systems (WECS) in the field of power quality assessment and distributed generation.

1 INTRODUCTION

1.1 Role of renewable energies in reducing greenhouse emissions

Increasing demand for energy, limited fossil fuel sources accompanied by rising prices, and a strong political opposition against nuclear power generation in many countries, have paid an increasing attention to alternative generation sources.

Renewable and sustainable energy sources, such as wind, solar, hydropower, biomass, geothermal, are becoming replacements for fossil fuels and primarily adopted by many countries due to the growing concern on global warming which is caused mainly by greenhouse emissions in fossil power stations.

Among the aforementioned renewable energy sources, the most utilized and notable for their contribution are solar, hydropower, and wind [1]-[3]. The most contributing of renewable energies is the sun; however, photovoltaic energy production is still expensive and requires further technical support [1]. On the other hand, hydroelectric power plants are inexpensive but have a limited life span; they cannot be widely utilized due to geographic limitations [4].

Wind is a clean, environmentally friendly, and inexhaustible available resource worldwide. Nowadays, wind power is the fastest-growing renewable energy source in the world with capacity doubling every three years [3], [5]. This fast development of wind energy has important implications for power systems engineers requiring a more complete understanding of the complexity of the positive and negative effects of wind energy in power systems.

1.2 Salient data of wind power around the world

The progress of wind power around the world has exceeded all the expectations, with Europe leading the global market. The capacity installed in Europe has increased with an average annual growth rate superior to 30% [5].

In 2013, wind generation produced nearly 4% of the world's electricity demand with 318.1 GW of wind power operating in 103 countries. Nearly 85% of the world's wind generating capacity resides in 21 countries participating in the International Energy Agency (IEA) [6]. Table 1.1 presents some statistics of the development of wind power in IEA member countries.

Table 1.1. Wind power statistics of the IEA member countries, 2013 [6].

Country	Total installed capacity (MW)	Total offshore installed capacity (MW)	Total number of turbines	Average capacity of new turbines (kW)	National electricity demand from wind (%)
Australia	3,239	0	1,651		4.1
Austria	1,684	0	113	2,730	5.8
Canada	7,803	0	4,377	2,000	3.1
China	91,413	428	63,120	1,719	2.6
Denmark	4,808	1271	5,194	3,132	32.7
Finland	448	26	210	3,200	0.9
Germany	34,660	903	23,864	On land 2,598 Offshore 4,485	8.9
Greece	1,865	0	1,357	1,145	5.8
Ireland	1,896	25			16.3
Italy	8,554	0	6,391	2,014	4.7
Japan	2,670	50	1,925	1,474	0.5
Korea	561	2	326	1,721	0.2
Mexico	1,551	0	1,071	2,000	1.5
Netherlands	2,709	228	2,160	2,729	4.7
Norway	811	2	356	2,500	1.4
Portugal	4,709	2	2,739	2,000	23.5
Spain	22,959	0	20,252	1,980	20.9
Sweden	4,469	0	2,681	2,912	7
Switzerland	60	0	34	2,216	0.2
United Kingdom	10,861	3653	5,413	-	6
United States	61,110	0	46,044	1,870	4.1

1.2.1 Wind power generation in Mexico

Mexico reached a total wind generation capacity of 1,551 MW during 2013, when 426 MW of new wind turbines were commissioned. Also, a 2,000 MW, 400 kV, 300 km electrical transmission line for wind energy projects in the Istmo de Tehuantepec was also commissioned in 2013 [7].

The Istmo de Tehuantepec in the Mexican state of Oaxaca is the largest wind energy resource region in Mexico with average annual wind speeds ranging from 7–10 m/s, measured at 30 m above the ground [7]. Also, it is estimated that more than 6,000 MW of wind power could be commercially tapped there [7].

The Mexican states of Baja California, Chiapas, Jalisco, Nuevo Leon, and Tamaulipas are emerging as the next wind energy deployment regions in Mexico [7].

1.3 WTG systems and power quality

Currently installed are wind turbine generators (WTGs) up to 7.5 MW and up to 140 m height [8], [9]. WTGs over 1 MW can involve either fixed- or variable-speed mainly with three blades and horizontal shaft. The driven electric generators are of synchronous or asynchronous type, though the predominant choice is the variable-speed doubly-fed induction generator (DFIG) system which provides benefits as only a proportion of the power passes through the converter. Compared to conventional variable-speed drives, the power converter in variable-speed DFIG systems represents approximately 30% in size, cost, and losses [1], [10], [11].

A main characteristic of the DFIG is that it does not have necessarily to be magnetized from the power grid, i.e., it can be magnetized from the rotor circuit. In addition, the DFIG is capable of generating reactive power that can be delivered to the stator via the grid-side converter [12].

In a DFIG-based WTG, the rotor windings are used as the secondary terminals of the generator to provide the capability of controlling the machine power, torque, speed, and reactive power. To control the abovementioned variables, the rotor-side converter (RSC) and the grid-side converter (GSC) are decoupled and controlled separately [4].

Traditionally, the rotor windings are supplied via an electronic power converter; thus producing current and voltage fluctuations combined with those caused by the aerodynamic behavior and wind speed variability.

Depending on the grid configuration and the type of wind turbine utilized, different power quality problems may arise, e.g., harmonic distortion, flickering, resonance effects, etc. Therefore, it is necessary to address the measurements to assess power quality of a grid-connected WTG as stated in the IEC 61400-21. In this respect the term power quality includes those electric characteristics of the WTG that influence the power quality of the grid to which the WTG is connected. The standard specifies the requirements for the measurement and assessment of the power, harmonic content, and flicker of grid-connected wind turbines.

1.4 Existent research on WTG with and without harmonics

Traditionally, power converters utilized in WTG systems are modeled via controllable voltage sources (CVSs) at fundamental frequency, i.e., neglecting harmonics which are essentially important to understand harmonic distortion, harmonic interaction phenomena, resonances, and power quality. A partial list of CVS-based WTG models is [13]-[18]. Very few studies, based on EMT-type simulation, focus on harmonic interaction analysis aimed to evaluate the control scheme and power quality assessment, e.g., [18], [19], noting that those studies require a post-processing algorithm to obtain harmonic frequencies from the instantaneous voltage/current waveforms.

1.5 Problem statement

WTGs require simulation studies aimed a) to analyze their interaction with the AC grid for control purposes, and b) to ensure a good performance under network disturbances. These studies require an accurate WTG dynamic model including mechanical and electrical subsystems.

Traditional WTG models do not address harmonic dynamics which represent a key point to understand instantaneous harmonic interaction phenomena, harmonic distortion, resonances, flickering, and power quality when connected to a grid. In most cases, the utilized back-to-back (BTB) converter is simplified and represented by using CVSs at fundamental frequency; thus, making difficult a detailed harmonic study when power converters are involved [18].

A major goal of the proposed EHD [20] model is to analyze harmonic frequencies in dynamic state of the WTG electrical and mechanical variables. Also, the EHD model accounts for harmonics in the BTB converter; thus, oscillations that may cause power converter problems and/or affect transient stability can be readily assessed. Although the proposed WTG model is formulated in the EHD, scheme controls such as PI, sliding-mode, or fuzzy-based control can be adopted due to any variable in the EHD can be readily transformed into the TD at any time instant. A WTG case study is presented and the obtained results are compared with those given by the PSCAD/EMTDC software tool [21].

2 MODELING HARMONICS IN POWER SYSTEMS

Voltages and currents in AC power systems are expected to be purely sinusoidal, with constant magnitude and phase. Nevertheless, generating power plants possess the undesirable property of introducing distortion into the AC power system [22], [23]. In addition, the inclusion of power electronics devices and nonlinear loads in power systems has become a major cause of harmonic distortion nowadays [23].

Harmonic distortion manifests as losses that shorten the lifetime of equipment like transformers and cables, interference in audio and data communication, tripping of overcurrent devices, overheating and vibrations in motors and transformers, resonance effects, overheating and fuse blowing of power-factor-correction capacitors, among others [22]-[24].

Periodic electrical signals can be decomposed into a set of sinusoidal waveforms of distinct magnitude and phase, and with frequencies that are multiples of the fundamental frequency (harmonics) [22]. That sinusoidal decomposition is also known as Fourier series.

2.1 Fourier series

Fourier series represent expansions of orthogonal functions usually used in power systems: 1) to extract the harmonic content of nonlinear characteristics when subjected to periodic excitations, and 2) to provide a generalized frame of reference where all the linear and nonlinear elements of the electric circuit are represented together [22].

A periodic signal $f(t)$ with period T_0 can be expanded into trigonometric Fourier series of the form

$$f(t) = \frac{1}{2}a_0 + \sum_{n=1}^{\infty} (a_n \cos n\omega_0 t + b_n \sin n\omega_0 t). \quad (2.1)$$

The coefficients of the series in (2.1) are given by

$$a_0 = \frac{2}{T_0} \int_{-T_0/2}^{T_0/2} f(t) dt, \quad (2.2)$$

$$a_n = \frac{2}{T_0} \int_{-T_0/2}^{T_0/2} f(t) \cos(n\omega_0 t) dt, \quad (2.3)$$

$$b_n = \frac{2}{T_0} \int_{-T_0/2}^{T_0/2} f(t) \sin(n\omega_0 t) dt \quad (2.4)$$

Equation (2.1) can also be represented in complex notation form by using the Euler's formulas:

$$\cos \varphi = \frac{1}{2} e^{j\varphi} + \frac{1}{2} e^{-j\varphi} \quad (2.5)$$

$$\sin \varphi = \frac{1}{2j} e^{j\varphi} - \frac{1}{2j} e^{-j\varphi} \quad (2.6)$$

Substituting (2.5) and (2.6) into (2.1) results in:

$$f(t) = \frac{a_0}{2} + \sum_{n=1}^{\infty} [C_n e^{jn\omega_0 t} + C_{-n} e^{-jn\omega_0 t}]. \quad (2.7)$$

Equation (2.7) can be rewritten as

$$f(t) = \sum_{n=-\infty}^{\infty} C_n e^{jn\omega_0 t} \quad (2.8)$$

which is known as the Fourier series in complex form. The complex coefficients of (2.8) are defined by

$$C_n = \frac{1}{T_0} \int_{-T_0/2}^{T_0/2} f(t) e^{-jn\omega_0 t} dt. \quad (2.9)$$

The derivative with respect to time of $f(t)$ is given by

$$f'(t) = \sum_{n=-\infty}^{\infty} jn\omega_0 C_n e^{jn\omega_0 t} \quad (2.10)$$

2.2 Harmonic domain (HD)

The HD is based on Fourier coefficients C_n arranged in a specific vector form given by

$$F = [C_{-h_{\max}} \cdots C_{-1} C_0 C_1 \cdots C_{h_{\max}}]^T \quad (2.11)$$

where h_{\max} corresponds to the maximum harmonic considered in the analysis and T denotes transposed. Any generic variable (voltage, current, flux) can be expressed in the HD using the corresponding arrangement, as in (2.11), to represent a periodic signal dictated by (2.8). Also, the derivative of a generic variable is given in the HD as

$$DF.$$

where D is given by a diagonal matrix with elements: $\{-jh_{\max}\omega_0, \dots, -j\omega_0, 0, j\omega_0, \dots, jh_{\max}\omega_0\}$;

An HD signal will be hereafter represented by capital letters and instantaneous TD variables by lowercase letters.

To illustrate the HD arrangement and the procedure to obtain the Fourier coefficients of an analytical function, consider the following TD analytical signal:

$$x(t) = 2 + \cos(\omega_0 t) + 0.2 \cos\left(2\omega_0 t + \frac{\pi}{8}\right) - 0.15 \cos\left(3\omega_0 t + \frac{\pi}{10}\right), \quad (2.12)$$

where ω_0 denotes the fundamental angular frequency in rad/s.

Using the Euler's identities (2.5) and (2.6), (2.12) can be rewritten in complex form as

$$x(t) = 2 + \frac{1}{2}(e^{j\omega_0 t} + e^{-j\omega_0 t}) + \frac{0.2}{2}\left(e^{j\frac{\pi}{8}}e^{j2\omega_0 t} + e^{-j\frac{\pi}{8}}e^{-j2\omega_0 t}\right) + \frac{0.15}{2}\left(e^{j\frac{\pi}{10}}e^{j3\omega_0 t} + e^{-j\frac{\pi}{10}}e^{-j3\omega_0 t}\right),$$

or,

$$x(t) = 2 + 0.5(e^{j\omega_0 t} + e^{-j\omega_0 t}) + (0.0924 + 0.0383j)e^{j2\omega_0 t} + (0.0924 - 0.0383j)e^{-j2\omega_0 t} + \dots \quad (2.13)$$

$$\dots + (-0.0713 - 0.0232j)e^{j3\omega_0 t} + (-0.0713 + 0.0232j)e^{-j3\omega_0 t}$$

Considering the coefficients of the exponential functions, and based on (2.11), (2.13) is represented in the HD as

$$X = \begin{bmatrix} X_{-3} \\ X_{-2} \\ X_{-1} \\ X_0 \\ X_1 \\ X_2 \\ X_3 \end{bmatrix} = \begin{bmatrix} -0.0713 + 0.0232j \\ 0.0924 - 0.0383j \\ 0.5 \\ 2 \\ 0.5 \\ 0.0924 + 0.0383j \\ -0.0713 - 0.0232j \end{bmatrix}. \quad (2.14)$$

In cases for which the analytical function is unknown but its corresponding TD-sampled signal is provided, the fast Fourier transform (FFT) algorithm can be used to obtain the corresponding Fourier coefficients. For example, consider that the signal (2.12), with $\omega_0 = 2\pi 50$ rad/s, is sampled using a sampling frequency of 500 Hz, Fig. 2.1. Application of the FFT algorithm to the sampled signal yields the same result as in (2.14).

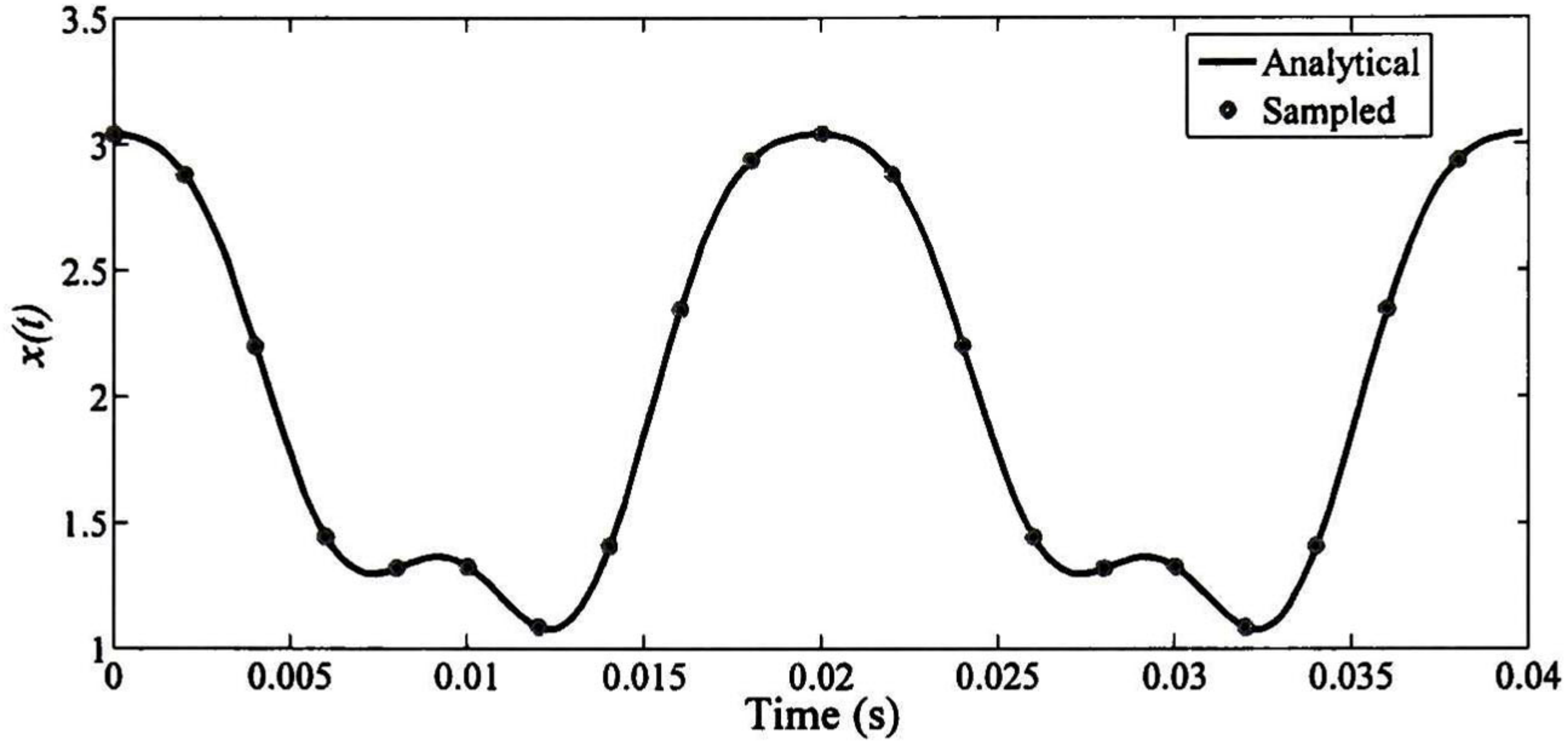


Fig. 2.1. Example of converting a TD signal into the HD.

2.2.1 Convolution in the HD

The HD convolution between two variables (or between the variable itself) is represented by the product of a Toeplitz-type matrix and an HD vector [22], both arranged as

$$X = \begin{bmatrix} X_{-h_{\max}} \\ \vdots \\ X_{-1} \\ X_0 \\ X_1 \\ \vdots \\ X_{h_{\max}} \end{bmatrix}; \quad X_{Toep} = \begin{bmatrix} X_0 & X_{-1} & \cdots & X_{-h_{\max}} & & & & \\ X_1 & X_0 & X_{-1} & \cdots & X_{-h_{\max}} & & & \\ \cdots & X_1 & X_0 & X_{-1} & \cdots & X_{-h_{\max}} & & \\ X_{h_{\max}} & \cdots & X_1 & X_0 & X_{-1} & \cdots & X_{-h_{\max}} & \\ & X_{h_{\max}} & \cdots & X_1 & X_0 & X_{-1} & \cdots & \\ & & X_{h_{\max}} & \cdots & X_1 & X_0 & X_{-1} & \\ & & & X_{h_{\max}} & \cdots & X_1 & X_0 & \end{bmatrix}. \quad (2.15)$$

As an illustrative example, consider the TD nonlinear relation given by

$$y(t) = x^4(t) + x^2(t). \quad (2.16)$$

Using (2.15), (2.16) is represented in the HD as

$$Y = X_{Toep}^3 X + X_{Toep} X, \quad (2.17)$$

where X and Y may represent HD vectors of mechanical/electrical variables.

The convolution concept outlined in this section can be applied to the HD representation of nonlinear loads expressed via polynomial relations in TD, e.g., magnetic saturation in transformers [22].

2.2.2 Linear elements in HD

The HD representations of the dynamic relations involving electrical linear elements are described next. Consider the TD relations for the R , L , and C elements, respectively:

$$v_R = Ri_R, \quad (2.18)$$

$$v_L = L \frac{di_L}{dt}. \quad (2.19)$$

$$v_C = \frac{1}{C} \int i_C dt. \quad (2.20)$$

From (2.18) to (2.20), the following HD relations are obtained

$$V_R = RI_R, \quad (2.21)$$

$$V_L = LDI_L, \quad (2.22)$$

$$V_C = \frac{1}{C} D^{-1} I_C. \quad (2.23)$$

2.2.3 Switching function in HD

Typically, electronic devices rely on switching elements with conducting and nonconducting periods of time within one fundamental frequency cycle. The dynamic relation between a switching function and an excitation can be represented as

$$v(t) = s(t)u(t), \quad (2.24)$$

where $s(t)$ represents the switching function and $u(t)$ denotes the excitation. The HD representation of (2.24) is given by

$$V = SU \quad (2.25)$$

In (2.25), S denotes a Toeplitz-type matrix with the harmonic content of $s(t)$ and U represents the HD vector corresponding to the excitation.

2.2.4 Steady-state solution via HD

The steady-state solution of a dynamic state-space system involves only the solution of a system of algebraic equations in the HD, as described next.

Consider for example the state-space system given by

$$\frac{d}{dt} \begin{bmatrix} x_1(t) \\ \vdots \\ x_m(t) \end{bmatrix} = \begin{bmatrix} a_1 \cdots s_1(t) \\ \vdots \quad \quad \quad \vdots \\ a_2 \cdots a_3 \end{bmatrix} \begin{bmatrix} x_1(t) \\ \vdots \\ x_m(t) \end{bmatrix} + \begin{bmatrix} s_2(t) \\ \vdots \\ b_1 \end{bmatrix} u(t), \quad (2.26)$$

where a_x denotes constant elements, s_x corresponds to switching functions, $x(t)$ are the states, and $u(t)$ represents a periodic excitation. Table 2.1 shows the representation of the distinct matrix elements in (2.26) in both TD and HD.

Table 2.1. Element representations in TD and HD.

	TD	HD
State	$x(t)$	X (vector form)
Excitation	$u(t)$	U (vector form)
Constant coefficient	a, b	aI, bI
Switching element	$s(t)$	S
Derivative	d/dt	D

Based on Table 2.1, the state-space system (2.26) becomes in the HD as

$$D \begin{bmatrix} X_1 \\ \vdots \\ X_m \end{bmatrix} = \begin{bmatrix} a_1 I \cdots S_1 \\ \vdots \quad \quad \quad \vdots \\ a_2 I \cdots a_3 I \end{bmatrix} \begin{bmatrix} X_1 \\ \vdots \\ X_m \end{bmatrix} + \begin{bmatrix} S_2 \\ \vdots \\ b_1 I \end{bmatrix} U, \quad (2.27)$$

where I denotes an identity matrix of appropriate dimensions; D corresponds to a set of identical differentiation matrices \mathcal{D} arranged in a block-diagonal form; S_x represents a Toeplitz-type matrix with the harmonic content of the switching function; U and X indicate the excitation and the states, respectively, represented as HD vectors. The solution of (2.27) provides the steady-state of the state-space system (2.26). Any HD quantity can be readily converted into TD via (2.8).

2.2.5 Example

This section has the objective of verification and validation of the outlined HD theory via a sample system.

A boost converter (BC), Fig. 2.2, is modeled in the HD, implemented in MatLab®, and compared with the PSCAD/EMTDC software tool [21]. The BC is a switch-mode DC-DC converter constituted by an inductor, two semiconductors (transistor and diode), and a capacitor, Fig. 2.2 (see Table 2.2 for parameter definitions). The main objective of the BC is to maintain a desired output voltage at the capacitor terminals by means of a PWM scheme in which the duty ratio (d) is the variable to be controlled.

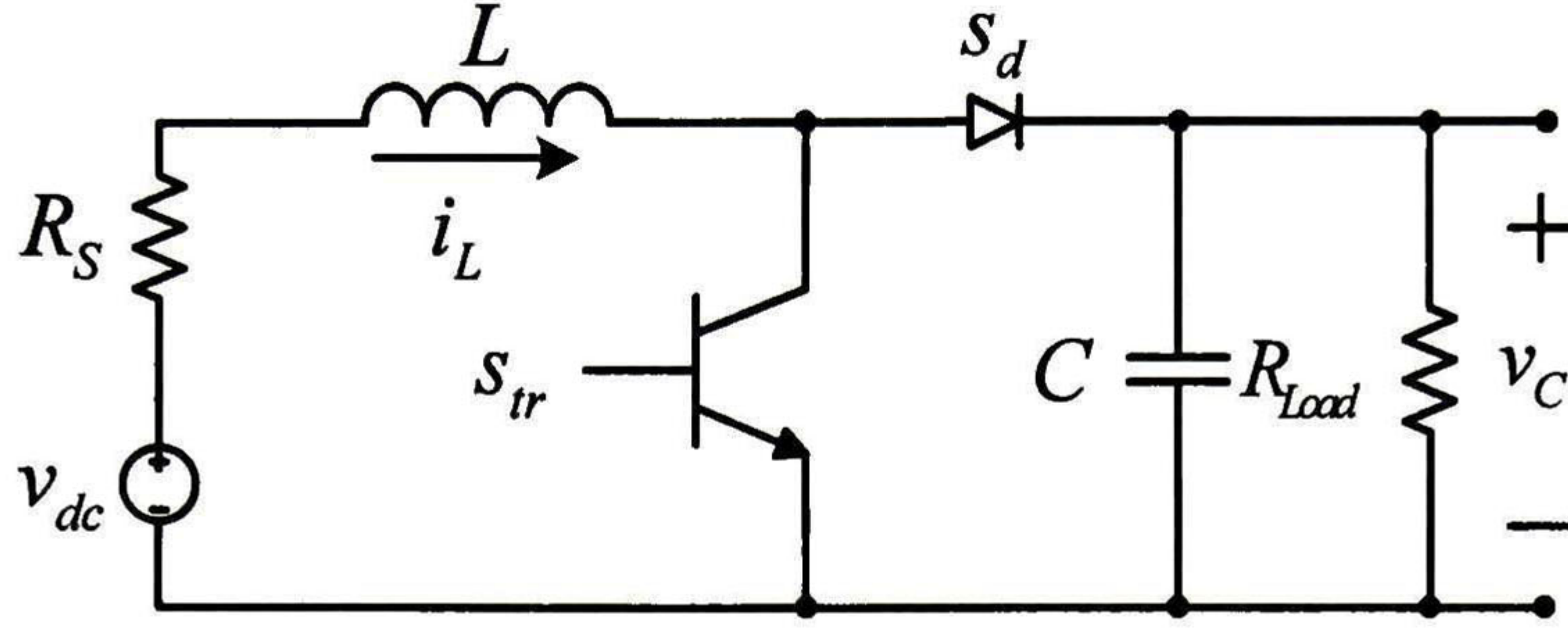


Fig. 2.2. Boost converter representation.

As an illustrative example of the switching function (s_{tr}) delivered by the PWM scheme, consider a duty cycle of 75% using a switching frequency of 2 kHz, Fig. 2.3.

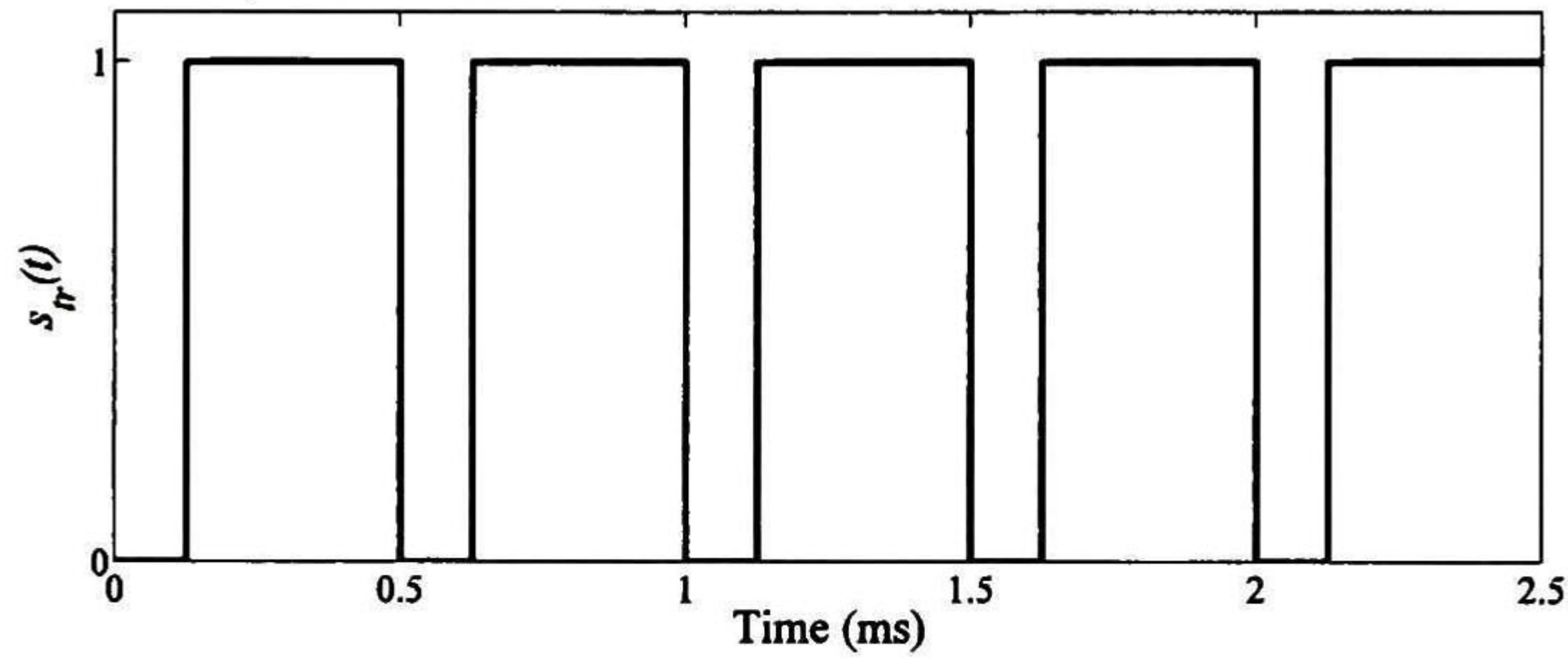


Fig. 2.3. Example of switching function.

The state-space representation of the BC, Fig. 2.2, is given by

$$\frac{d}{dt} \begin{bmatrix} v_C(t) \\ i_L(t) \end{bmatrix} = \begin{bmatrix} -\frac{1}{R_{Load}C} & \frac{1}{C}s_d(t) \\ -\frac{1}{L}s_d(t) & -\frac{R_S}{L} \end{bmatrix} \begin{bmatrix} v_C(t) \\ i_L(t) \end{bmatrix} + \begin{bmatrix} 0 \\ \frac{1}{L} \end{bmatrix} v_{dc}, \quad (2.28)$$

where the diode conduction time is given by

$$s_d(t) = 1 - s_{tr}(t),$$

where subscripts d and tr denote diode and transistor, respectively.

Based on the HD theory described in this Chapter, (2.28) is converted into the HD resulting in:

$$D \begin{bmatrix} V_C \\ I_L \end{bmatrix} = \begin{bmatrix} -\frac{1}{R_{Load}C} I & \frac{1}{C} S_d \\ -\frac{1}{L} S_d & -\frac{R_S}{L} I \end{bmatrix} \begin{bmatrix} V_C \\ I_L \end{bmatrix} + \begin{bmatrix} 0 \\ \frac{1}{L} I \end{bmatrix} V_{dc}, \quad (2.29)$$

where S_d is a Toeplitz-type matrix with the corresponding harmonic content of the switching function.

The solution of (2.29) provides the stationary state for the voltage at the capacitor terminals and the current across the inductor, i.e., V_C and I_L , respectively. The harmonic content of these two variables are presented in Fig. 2.4, where insets represent their corresponding close-up.

The results in Fig. 2.4 show a very good agreement between the HD model and the PSCAD/EMTDC results. The parameters of the simulated system are shown in Table 2.2.

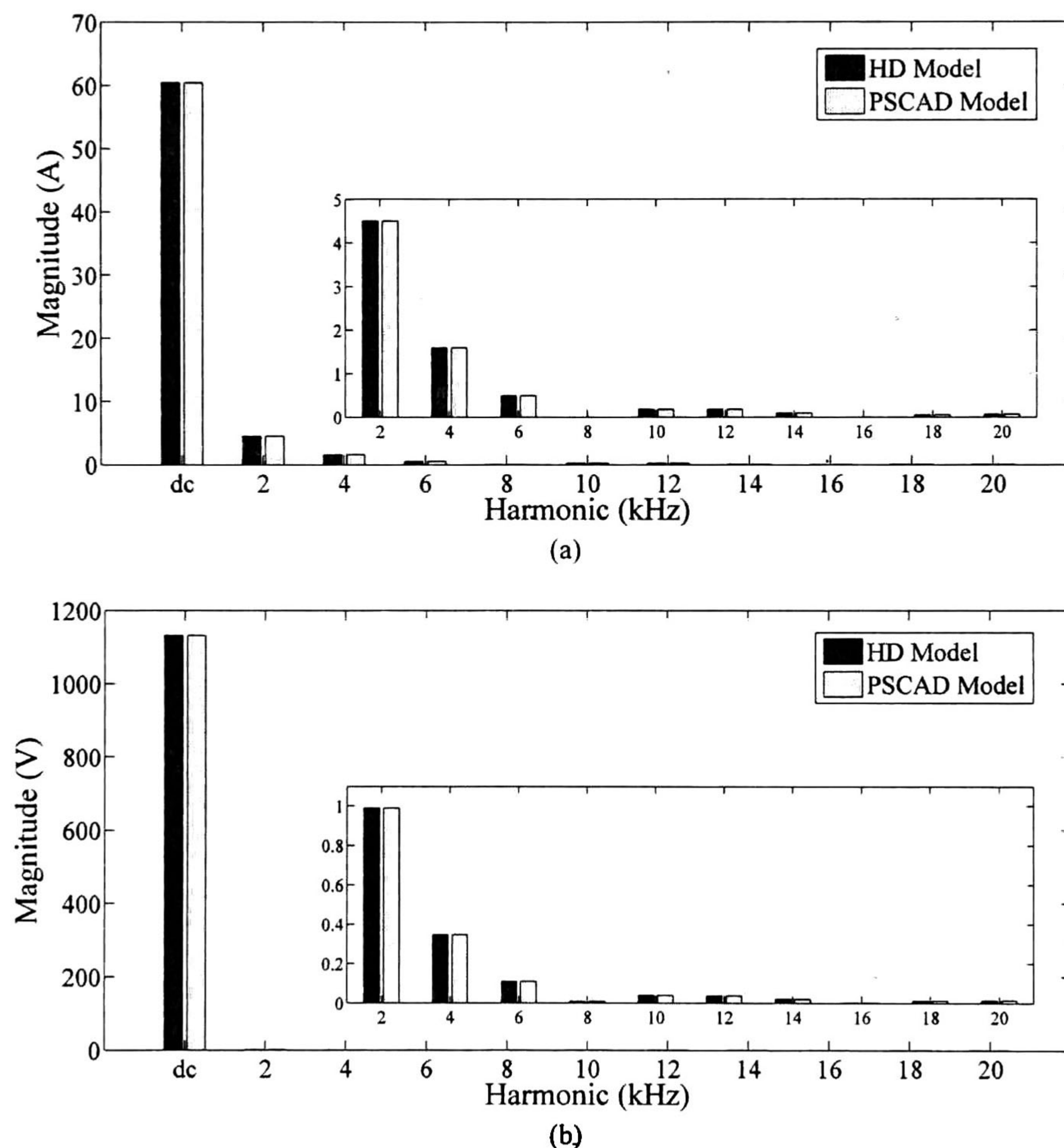


Fig. 2.4. Simulation results a) Current across inductor b) Voltage at capacitor terminals.

Table 2.2. Parameters of the BC simulation.

Boost converter system		
C	2200 μF	Capacitor
L	9 mH	Inductance
R_{Load}	25 Ω	Load
R_S	2.5 Ω	Source resistance
v_{dc}	1 kV	DC voltage
d	0.25	Duty cycle
f_{sw}	2 kHz	Switching frequency

2.3 Extended harmonic domain (EHD)

The EHD method considers that harmonics vary slowly with respect to time within a period [20], contrary to the HD method which considers the harmonics as constants. In the EHD, a variable $x(t)$ and its derivative $\dot{x}(t)$ are represented as

$$x(t) = \sum_{n=-\infty}^{\infty} C_n(t) e^{jn\omega_0 t} \quad (2.30)$$

$$\dot{x}(t) = \sum_{n=-\infty}^{\infty} \dot{C}_n(t) e^{jn\omega_0 t} + \sum_{n=-\infty}^{\infty} jn\omega_0 C_n(t) e^{jn\omega_0 t} = \sum_{n=-\infty}^{\infty} [\dot{C}_n(t) + jn\omega_0 C_n(t)] e^{jn\omega_0 t}$$

The corresponding EHD images of $x(t)$ and $\dot{x}(t)$ are:

$$x(t) \Rightarrow X, \quad (2.31)$$

$$\dot{x}(t) \Rightarrow \dot{X} + DX. \quad (2.32)$$

Based on (2.31) and (2.32), the EHD state-space representation of the state-space system (2.26) is given by

$$\frac{d}{dt} \begin{bmatrix} X_1 \\ \vdots \\ X_m \end{bmatrix} + D \begin{bmatrix} X_1 \\ \vdots \\ X_m \end{bmatrix} = \begin{bmatrix} a_1 I & \cdots & S_1 \\ \vdots & \ddots & \vdots \\ a_2 I & \cdots & a_3 I \end{bmatrix} \begin{bmatrix} X_1 \\ \vdots \\ X_m \end{bmatrix} + \begin{bmatrix} S_2 \\ \vdots \\ b_1 I \end{bmatrix} U. \quad (2.33)$$

Note that (2.33) provides the dynamics of harmonics and can be solved by using any numerical integration method when required (an analytical solution may exist). Any EHD variable can be readily transformed into the TD by using (2.30).

2.3.1 Example

This section presents the comparison of the HD, EHD, and TD models of the BC shown in Fig. 2.2. Based on (2.28) and (2.33), the EHD model of the BC is given by

$$\frac{d}{dt} \begin{bmatrix} V_C \\ I_L \end{bmatrix} + D \begin{bmatrix} V_C \\ I_L \end{bmatrix} = \begin{bmatrix} -\frac{1}{R_{Load}C} I & \frac{1}{C} S_d \\ -\frac{1}{L} S_d & -\frac{R_S}{L} I \end{bmatrix} \begin{bmatrix} V_C \\ I_L \end{bmatrix} + \begin{bmatrix} 0 \\ \frac{1}{L} I \end{bmatrix} V_{dc}. \quad (2.34)$$

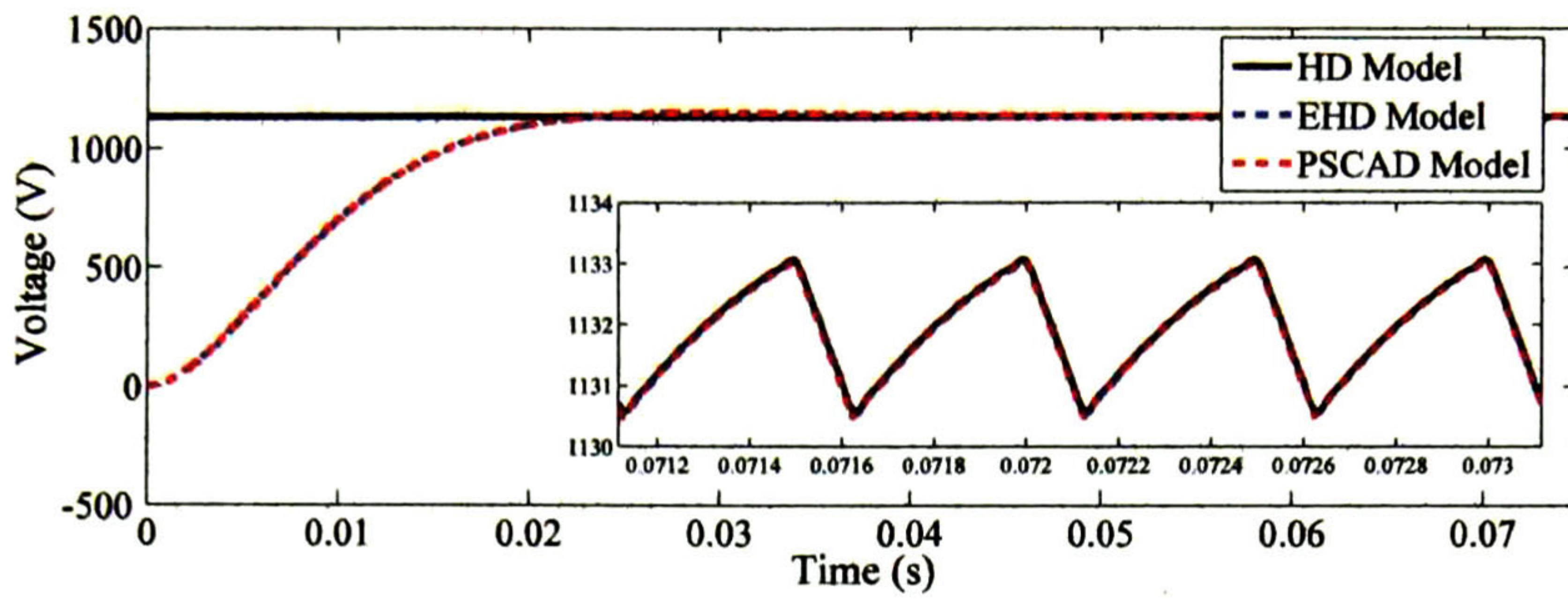
The numerical solution of the EHD model, given by (2.34), is efficiently performed by using the trapezoidal integration method. On the other hand, the steady-state of the BC is calculated by solving (2.29). Also, the BC is programmed under the PSCAD/EMTDC environment. Assuming zero initial conditions, the instantaneous voltage at capacitor terminals v_C and the current across the inductor i_L , given by the three models, are shown in Fig. 2.5. Fig. 2.5 shows a remarkable agreement between the EHD and PSCAD results which converge to the steady-state solution by the HD model.

Fig. 2.5(c) and Fig. 2.5(d) present the corresponding harmonic evolution with respect to time of the computed variables, obtained with the EHD model. The harmonics dynamics by the EHD model can be used to calculate instantaneous power quality indices. On the other hand, the PSCAD/EMTDC solution requires a post-processing routine to obtain harmonics dynamics which in fact provides inaccurate results due to the implicit error incurred by the windowed Fourier transform (WFT) [25].

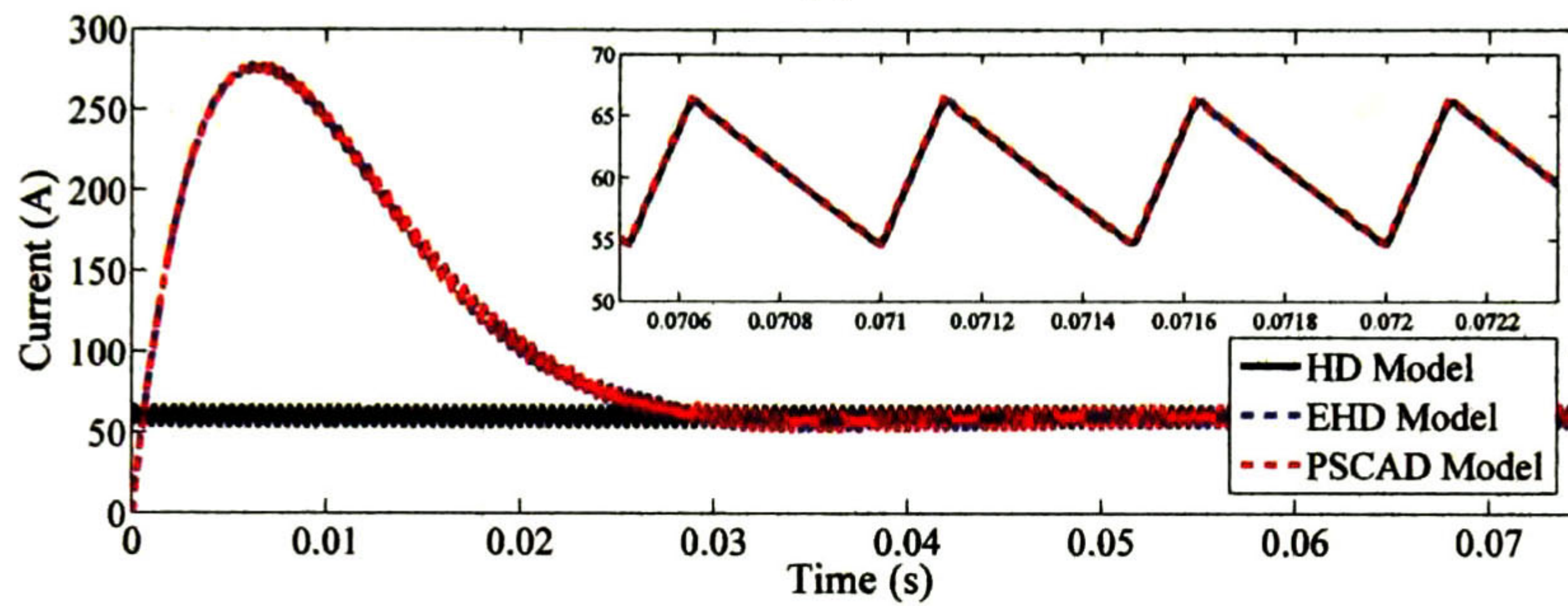
Table 2.3 presents the simulation data used for this example, including the CPU times by the HD and EHD models and the PSCAD/EMTDC simulation. Table 2.3 shows that the HD requires the smallest CPU time; this is due to the direct solution of a system of algebraic equations, as in (2.29). Also, Table 2.3 shows that the EHD model requires less CPU time than the PSCAD/EMTDC simulation accounting that the EHD is programmed in a distinct (slower) platform than PSCAD/EMTDC. The latter would require an additional CPU time to obtain harmonics dynamics.

Table 2.3. Simulation data of the BC simulation.

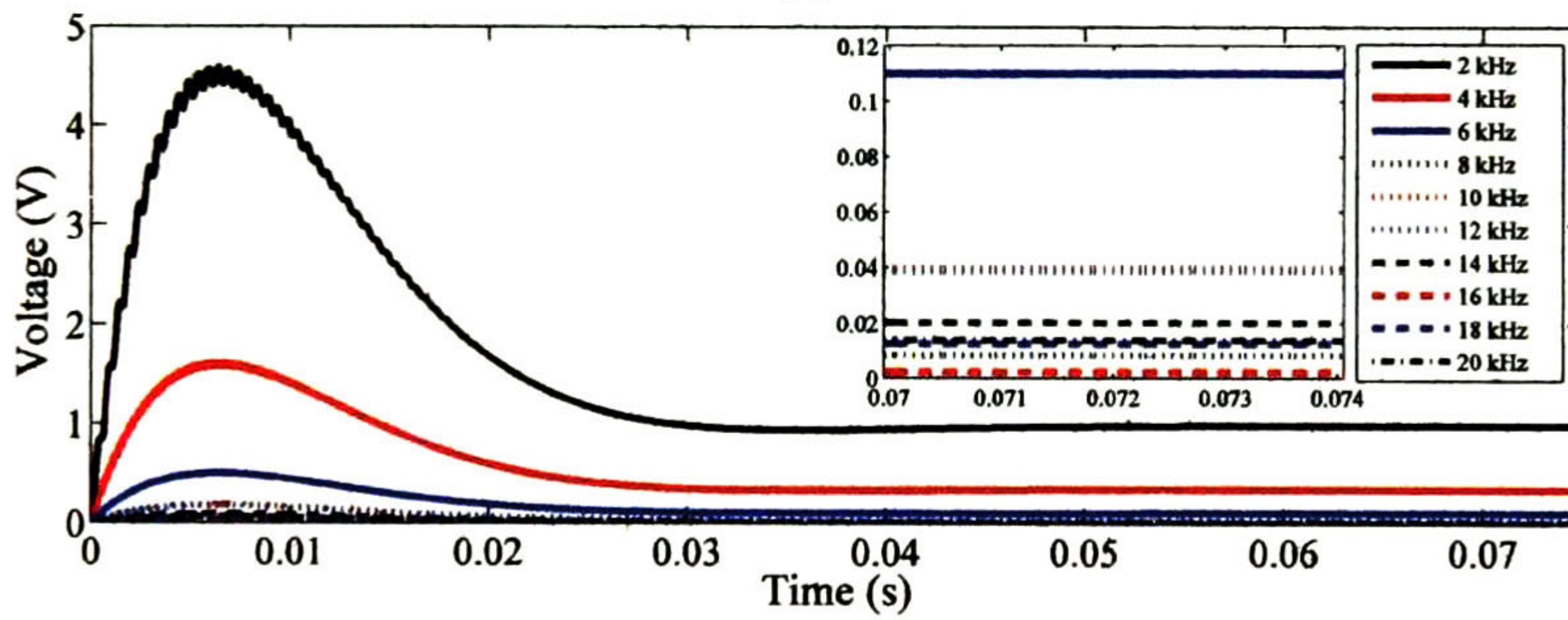
	HD model (MatLab®)	EHD model (MatLab®)	PSCAD/EMTDC
Simulation time frame (s)	0.075		
Δt (μ s)	-	1	1
CPU time (s)	0.000671	1.4171	4.03
Harmonics	1-10		-
Switching freq.	2 kHz		
Fundamental freq.	2 kHz		



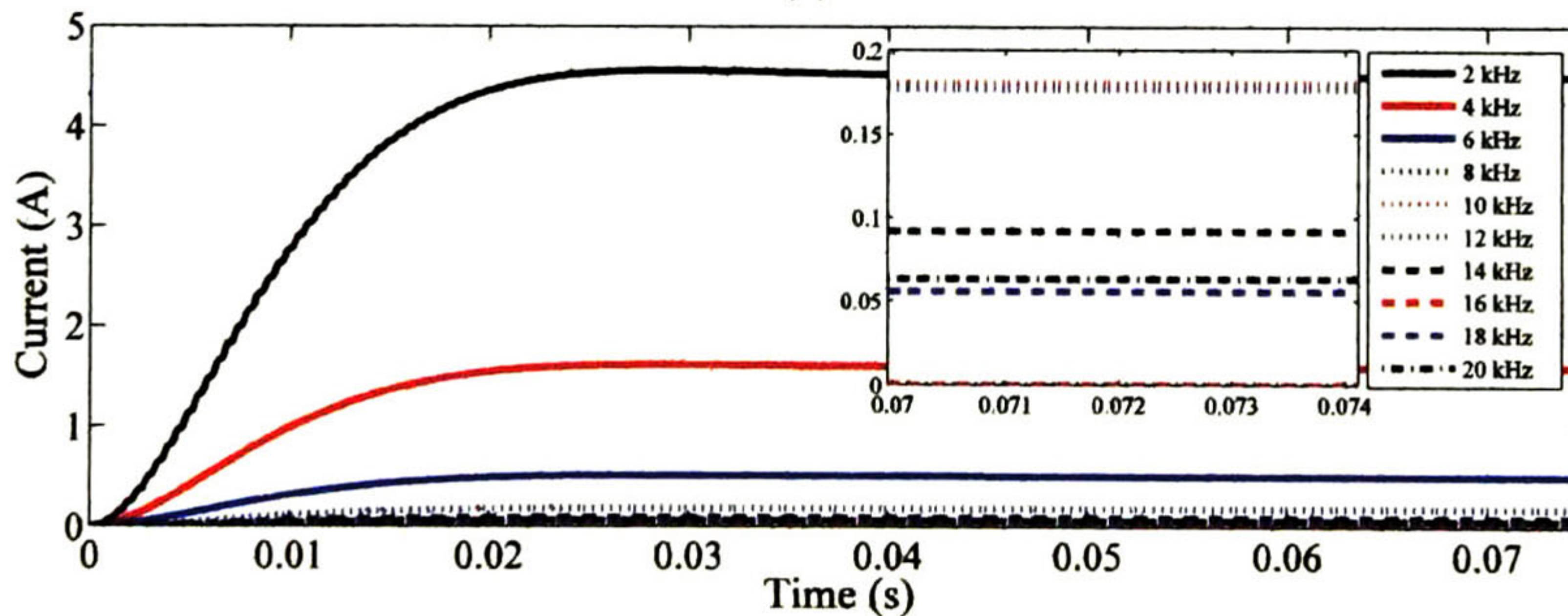
(a)



(b)



(c)



(d)

Fig. 2.5. Simulation results a) Voltage at capacitor terminals b) Current across inductor c) Harmonic evolution of v_C d) Harmonic evolution of i_L .

2.4 Conclusions

The basic theories of the HD and the EHD have been reviewed. Linear and nonlinear element representations have been defined in both HD and EHD.

A remarkable characteristic of the EHD model is the availability of instantaneous time-variation harmonics, mainly used for power quality assessment purposes. On the contrary, the PSCAD/EMTDC software tool requires a post-processing procedure to obtain the harmonic content, i.e., using a windowed FFT algorithm [21], [25].

A major feature of the HD model is the direct computation of steady-state. On the contrary, software tools like PSCAD/EMTDC have to simulate a large time frame to allow the transient damps out. Hence, the HD can be employed for initialization in EMT-type software tools.

3 WTG EHD MODEL

This Chapter presents the modeling of a WTG in the EHD, including both electrical and mechanical parts. The electrical subsystem includes the DFIG, back-to-back (BTB) converter, AC grid, and the RL filter, whereas the mechanical subsystem is constituted by the aerodynamic and the torsional shaft models. The WTG is assumed to be controlled via a two-level scheme control aimed to improve the WTG performance and quality of power conversion.

3.1 General description

A schematic representation of the WTG system considered in this thesis is shown in Fig. 3.1. The turbine rotor of the WTG is coupled to the DFIG through a shaft system. Also, as shown in Fig. 3.1, the DFIG rotor and stator windings are fed by the BTB converter and the grid, respectively.

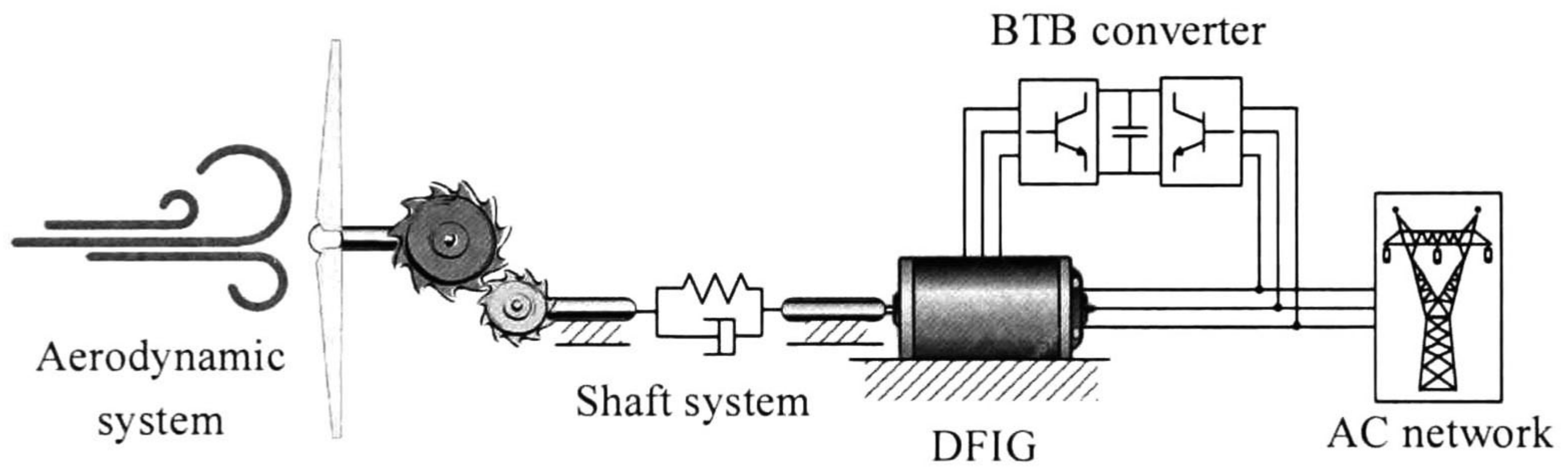


Fig. 3.1. Schematic representation of the WTG system.

3.2 DFIG EHD model

This thesis assumes the DFIG having three identical and symmetrically spaced windings in both stator and rotor. Under this idealized model, expressed in motor convention, the instantaneous stator and rotor voltages and currents are described by [11]

$$\vec{v}_{abc_s}^{-s} = r_{abc_s} \vec{i}_{abc_s}^{-s} + \frac{d}{dt} \vec{\psi}_{abc_s}^{-s} \quad (3.1)$$

$$\vec{v}_{abc_r}^{-r} = r_{abc_r} \vec{i}_{abc_r}^{-r} + \frac{d}{dt} \vec{\psi}_{abc_r}^{-r} \quad (3.2)$$

where subscripts s and r denote stator and rotor variables, whereas superscripts correspond to the stator and rotor reference frames, respectively; r_{abc_s} and r_{abc_r} are given by diagonal matrices with elements: $\{r_s, r_s, r_s\}$ and $\{r_r, r_r, r_r\}$, respectively.

In this thesis, the stator ($\alpha\beta$) reference frame is used due to the main characteristic that the stator and rotor variables rotate at synchronous speed (ω_s) [11]. This allows having components rotating at fundamental frequency and their harmonics. See Appendix for the basic theory of reference frames.

The referring of (3.1) to the $\alpha\beta$ -reference frame is achieved by the next operations (see Appendix for definition of $T_{\alpha\beta}$ and basic theory of transformation from abc - to $\alpha\beta$ -reference frame):

$$\begin{aligned} T_{\alpha\beta}^{-1} \vec{v}_{\alpha\beta_s} &= r_{abc_s} T_{\alpha\beta}^{-1} \vec{i}_{\alpha\beta_s} + \frac{d}{dt} T_{\alpha\beta}^{-1} \vec{\psi}_{\alpha\beta_s}, \\ \vec{v}_{\alpha\beta_s} &= r_{\alpha\beta_s} \vec{i}_{\alpha\beta_s} + \frac{d}{dt} \vec{\psi}_{\alpha\beta_s}, \end{aligned} \quad (3.3)$$

where $r_{\alpha\beta_s}$ denotes a diagonal matrix with elements: $\{r_s, r_s\}$.

As for the rotor equation (3.2), it is first transformed to the DQ -reference frame (see Appendix for definition of T_{DQ} and basic theory of transformation from abc - to DQ -reference frame), as follows:

$$\begin{aligned} T_{DQ}^{-1} \vec{v}_{DQ_r} &= r_{abc_r} T_{DQ}^{-1} \vec{i}_{DQ_r} + \frac{d}{dt} T_{DQ}^{-1} \vec{\psi}_{DQ_r}, \\ \vec{v}_{DQ_r} &= r_{DQ_r} \vec{i}_{DQ_r} + \frac{d}{dt} \vec{\psi}_{DQ_r} \end{aligned} \quad (3.4)$$

Then, the rotor equation is transformed from DQ - to the $\alpha\beta$ -reference frame by the next operations (see Appendix for definition of M and basic theory of transformation from DQ - to $\alpha\beta$ -reference frame):

$$\begin{aligned} M^{-1} \vec{v}_{\alpha\beta_r} &= r_{DQ_r} M^{-1} \vec{i}_{\alpha\beta_r} + \frac{d}{dt} \left(M^{-1} \vec{\psi}_{\alpha\beta_r} \right), \\ \vec{v}_{\alpha\beta_r} &= r_{\alpha\beta_r} \vec{i}_{\alpha\beta_r} - j\omega_{\alpha\beta_m} \vec{\psi}_{\alpha\beta_r} + \frac{d}{dt} \left(\vec{\psi}_{\alpha\beta_r} \right). \end{aligned} \quad (3.5)$$

In (3.4) and (3.5), r_{DQ_r} and $r_{\alpha\beta_r}$ correspond to a diagonal matrix with elements: $\{r_r, r_r\}$; $\omega_{\alpha\beta_m}$ is given by a diagonal matrix with elements: $\{\omega_m, \omega_m\}$.

Rewriting (3.3) and (3.5) in matrix form gives

$$\begin{bmatrix} \bar{v}_{\alpha\beta_s} \\ \bar{v}_{\alpha\beta_r} \end{bmatrix} = \begin{bmatrix} r_{\alpha\beta_s} & 0 \\ 0 & r_{\alpha\beta_r} \end{bmatrix} \begin{bmatrix} \bar{i}_{\alpha\beta_s} \\ \bar{i}_{\alpha\beta_r} \end{bmatrix} + \begin{bmatrix} 0 & 0 \\ 0 & -j\omega_{\alpha\beta_m} \end{bmatrix} \begin{bmatrix} \bar{\psi}_{\alpha\beta_s} \\ \bar{\psi}_{\alpha\beta_r} \end{bmatrix} + \frac{d}{dt} \begin{bmatrix} \bar{\psi}_{\alpha\beta_s} \\ \bar{\psi}_{\alpha\beta_r} \end{bmatrix}. \quad (3.6)$$

On the other hand, the relation between fluxes and currents is given by

$$\begin{bmatrix} \bar{\psi}_{\alpha\beta_s} \\ \bar{\psi}_{\alpha\beta_r} \end{bmatrix} = \begin{bmatrix} L_{\alpha\beta_s} & L_{\alpha\beta_m} \\ L_{\alpha\beta_m} & L_{\alpha\beta_r} \end{bmatrix} \begin{bmatrix} \bar{i}_{\alpha\beta_s} \\ \bar{i}_{\alpha\beta_r} \end{bmatrix}, \quad (3.7)$$

where $L_{\alpha\beta_s}$, $L_{\alpha\beta_r}$, and $L_{\alpha\beta_m}$ indicate diagonal matrices with elements: $\{L_s, L_s\}$, $\{L_r, L_r\}$, and $\{L_m, L_m\}$, respectively.

Substituting (3.7) into (3.6) gives

$$\begin{aligned} \begin{bmatrix} \bar{v}_{\alpha\beta_s} \\ \bar{v}_{\alpha\beta_r} \end{bmatrix} &= \begin{bmatrix} r_{\alpha\beta_s} & 0 \\ 0 & r_{\alpha\beta_r} \end{bmatrix} \begin{bmatrix} \bar{i}_{\alpha\beta_s} \\ \bar{i}_{\alpha\beta_r} \end{bmatrix} + \begin{bmatrix} 0 & 0 \\ 0 & -j\omega_{\alpha\beta_m} \end{bmatrix} \begin{bmatrix} L_{\alpha\beta_s} & L_{\alpha\beta_m} \\ L_{\alpha\beta_m} & L_{\alpha\beta_r} \end{bmatrix} \begin{bmatrix} \bar{i}_{\alpha\beta_s} \\ \bar{i}_{\alpha\beta_r} \end{bmatrix} + \frac{d}{dt} \begin{bmatrix} L_{\alpha\beta_s} & L_{\alpha\beta_m} \\ L_{\alpha\beta_m} & L_{\alpha\beta_r} \end{bmatrix} \begin{bmatrix} \bar{i}_{\alpha\beta_s} \\ \bar{i}_{\alpha\beta_r} \end{bmatrix}, \\ \frac{d}{dt} \begin{bmatrix} \bar{i}_{\alpha\beta_s} \\ \bar{i}_{\alpha\beta_r} \end{bmatrix} &= \begin{bmatrix} L_{\alpha\beta_s} & L_{\alpha\beta_m} \\ L_{\alpha\beta_m} & L_{\alpha\beta_r} \end{bmatrix}^{-1} \left(\begin{bmatrix} \bar{v}_{\alpha\beta_s} \\ \bar{v}_{\alpha\beta_r} \end{bmatrix} - \begin{bmatrix} r_{\alpha\beta_s} & 0 \\ 0 & r_{\alpha\beta_r} \end{bmatrix} \begin{bmatrix} \bar{i}_{\alpha\beta_s} \\ \bar{i}_{\alpha\beta_r} \end{bmatrix} + \begin{bmatrix} 0 & 0 \\ 0 & j\omega_{\alpha\beta_m} \end{bmatrix} \begin{bmatrix} L_{\alpha\beta_s} & L_{\alpha\beta_m} \\ L_{\alpha\beta_m} & L_{\alpha\beta_r} \end{bmatrix} \begin{bmatrix} \bar{i}_{\alpha\beta_s} \\ \bar{i}_{\alpha\beta_r} \end{bmatrix} \right), \\ \frac{d}{dt} \begin{bmatrix} \bar{i}_{\alpha\beta_s} \\ \bar{i}_{\alpha\beta_r} \end{bmatrix} &= \frac{1}{L_s L_r - L_m^2} \left(\begin{bmatrix} L_{\alpha\beta_s} & -L_{\alpha\beta_m} \\ -L_{\alpha\beta_m} & L_{\alpha\beta_r} \end{bmatrix} \begin{bmatrix} \bar{v}_{\alpha\beta_s} \\ \bar{v}_{\alpha\beta_r} \end{bmatrix} + \dots \right. \\ &\quad \left. \dots + \begin{bmatrix} -r_{\alpha\beta_s} L_{\alpha\beta_r} - j\omega_m L_{\alpha\beta_m}^2 & r_{\alpha\beta_r} L_{\alpha\beta_m} - j\omega_m L_{\alpha\beta_m} L_{\alpha\beta_s} \\ r_{\alpha\beta_s} L_{\alpha\beta_m} + j\omega_m L_{\alpha\beta_m} L_{\alpha\beta_s} & -r_{\alpha\beta_r} L_{\alpha\beta_s} + j\omega_m L_{\alpha\beta_s} L_{\alpha\beta_r} \end{bmatrix} \begin{bmatrix} \bar{i}_{\alpha\beta_s} \\ \bar{i}_{\alpha\beta_r} \end{bmatrix} \right) \end{aligned} \quad (3.8)$$

Note that the product of two generic vectors expressed in complex form can be expanded in $\alpha\beta$ -components by next operations:

$$\begin{aligned} \bar{x}_{\alpha\beta} = (a + jb) \bar{y}_{\alpha\beta} &\Rightarrow (x_\alpha + jx_\beta) = (a + jb)(y_\alpha + jy_\beta), \\ \begin{bmatrix} x_\alpha \\ x_\beta \end{bmatrix} &= \begin{bmatrix} a & -b \\ b & a \end{bmatrix} \begin{bmatrix} y_\alpha \\ y_\beta \end{bmatrix}. \end{aligned} \quad (3.9)$$

Applying (3.9) into (3.8), the DFIG model in compact form is given by

$$\frac{d}{dt} \begin{bmatrix} i_{\alpha_s} \\ i_{\beta_s} \\ i_{\alpha_r} \\ i_{\beta_r} \end{bmatrix} = \frac{1}{L_s L_r - L_m^2} \left(L_1 \begin{bmatrix} i_{\alpha_s} \\ i_{\beta_s} \\ i_{\alpha_r} \\ i_{\beta_r} \end{bmatrix} + L_2 \begin{bmatrix} v_{\alpha_s} \\ v_{\beta_s} \\ v_{\alpha_r} \\ v_{\beta_r} \end{bmatrix} \right), \quad (3.10)$$

where:

$$L_1 = \begin{bmatrix} -r_s L_r & \omega_m L_m^2 & r_r L_m & \omega_m L_m L_r \\ -\omega_m L_m^2 & -r_s L_r & -\omega_m L_m L_r & r_r L_m \\ r_s L_m & -\omega_m L_m L_s & -r_r L_s & -\omega_m L_s L_r \\ \omega_m L_m L_s & r_s L_m & \omega_m L_s L_r & -r_r L_s \end{bmatrix}, \quad (3.11)$$

$$L_2 = \begin{bmatrix} L_r & 0 & -L_m & 0 \\ 0 & L_r & 0 & -L_m \\ -L_m & 0 & L_s & 0 \\ 0 & -L_m & 0 & L_s \end{bmatrix}, \quad (3.12)$$

$$L_s = L_{ls} + L_m, \quad (3.13)$$

$$L_r = L_{lr} + L_m. \quad (3.14)$$

In (3.10) to (3.14), L_{ls} and L_{lr} denote the leakage inductances, and r_s and r_r represent the resistances, corresponding to stator and rotor, respectively; L_m corresponds to the magnetizing inductance; ω_m indicates the electric rotational speed.

The electromagnetic torque of the DFIG is given in $\alpha\beta$ -coordinates by

$$T_e = \frac{3}{2} L_m P (i_{\beta_s} i_{\alpha_r} - i_{\alpha_s} i_{\beta_r}). \quad (3.15)$$

Based on the theory of Chapter 2, the state-space of the DFIG EHD model in $\alpha\beta$ -coordinates is obtained converting (3.10) to (3.15) into the EHD, resulting in:

$$\frac{d}{dt} \begin{bmatrix} I_{\alpha_s} \\ I_{\beta_s} \\ I_{\alpha_r} \\ I_{\beta_r} \end{bmatrix} + D \begin{bmatrix} I_{\alpha_s} \\ I_{\beta_s} \\ I_{\alpha_r} \\ I_{\beta_r} \end{bmatrix} = \frac{1}{L_s L_r - L_m^2} \left(L_1 \begin{bmatrix} I_{\alpha_s} \\ I_{\beta_s} \\ I_{\alpha_r} \\ I_{\beta_r} \end{bmatrix} + L_2 \begin{bmatrix} V_{\alpha_s} \\ V_{\beta_s} \\ V_{\alpha_r} \\ V_{\beta_r} \end{bmatrix} \right), \quad (3.16)$$

where L_1 and L_2 are defined in the HD as

$$L_1 = \begin{bmatrix} -r_s L_r I & \omega_{m_{Toep}} L_m^2 & r_r L_m I & \omega_{m_{Toep}} L_m L_r \\ -\omega_{m_{Toep}} L_m^2 & -r_s L_r I & -\omega_{m_{Toep}} L_m L_r & r_r L_m I \\ r_s L_m I & -\omega_{m_{Toep}} L_m L_s & -r_r L_s I & -\omega_{m_{Toep}} L_s L_r \\ \omega_{m_{Toep}} L_m L_s & r_s L_m I & \omega_{m_{Toep}} L_s L_r & -r_r L_s I \end{bmatrix}, \quad (3.17)$$

$$L_2 = \begin{bmatrix} L_r I & 0 & -L_m I & 0 \\ 0 & L_r I & 0 & -L_m I \\ -L_m I & 0 & L_s I & 0 \\ 0 & -L_m I & 0 & L_s I \end{bmatrix}. \quad (3.18)$$

The electromagnetic torque given by (3.15), is defined in the HD as

$$T_e = \frac{3}{2} L_m P \begin{bmatrix} I_{\beta s_{Toep}} & -I_{\alpha s_{Toep}} \end{bmatrix} \begin{bmatrix} I_{\alpha_r} \\ I_{\beta_r} \end{bmatrix}. \quad (3.19)$$

In (3.17) and (3.19), subscript *Toep* denotes a Toeplitz-type matrix, and P is the pole pairs.

3.3 Aerodynamic EHD model

The aerodynamic system represents the power extraction from the turbine, providing the mechanical torque as function of the air flow on the blades. The wind speed can be considered as the averaged incident wind speed over the area swept by the blades [11].

The mechanical torque generated by a typical turbine can be defined in the EHD by

$$T_{tur} = \frac{\rho \pi R^3 V_w^2 C_p \lambda^{-1}}{2}. \quad (3.20)$$

$$\lambda = \frac{R \Omega_{tur_{Toep}}}{V_w} \quad (3.21)$$

In (3.20) and (3.21), R represents the length of the blades (m), V_w corresponds to the wind speed (m/s), ρ denotes the air density (kg/m^3), Ω_{tur} is the mechanical speed of the turbine (rad/s), λ is defined as the tip speed ratio, and C_p indicates the power coefficient.

To compare the results of the proposed WTG EHD system, Fig. 3.1, with the PSCAD/EMTDC software tool, the power coefficient in this thesis corresponds to the one in the wind turbine block of PSCAD/EMTDC, Fig. 3.2. Also, both models take into account the gear ratio.

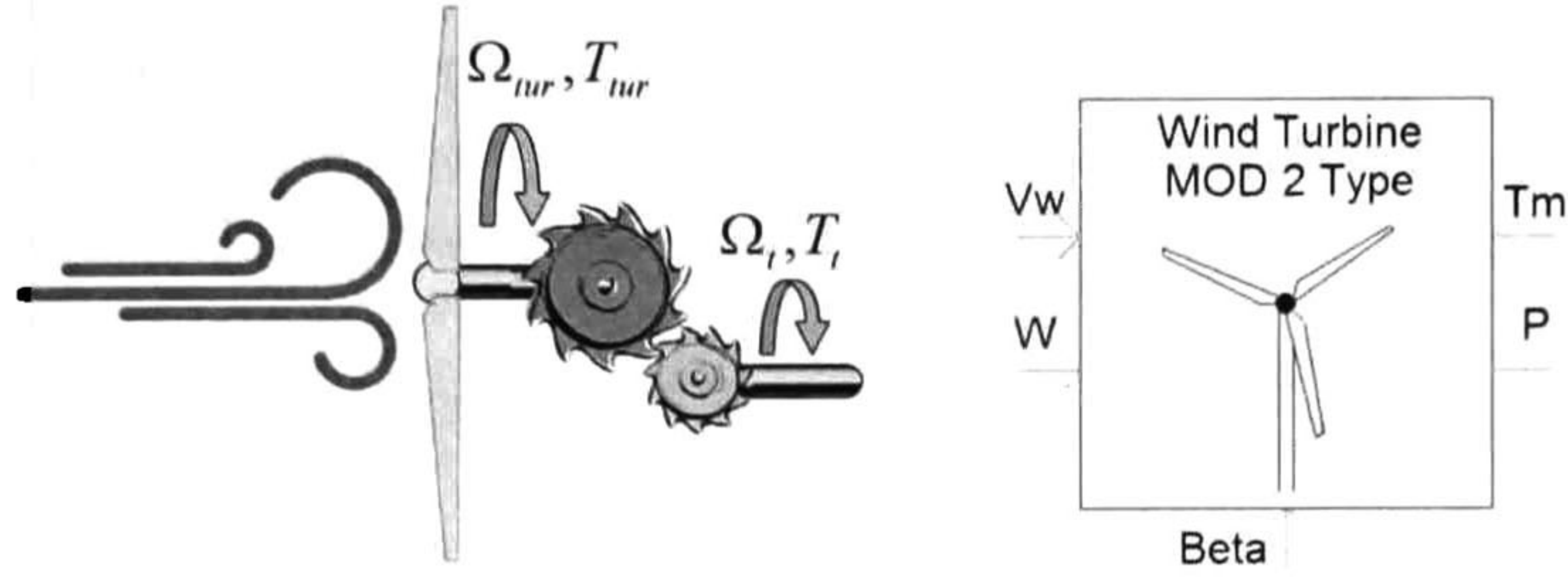


Fig. 3.2. Aerodynamic representation - PSCAD/EMTDC block.

The aforementioned power coefficient is given in the EHD by

$$C_p = 0.5(\gamma_{Toep} - 0.022\beta^2 I - 5.6I)e^{-0.17\gamma} \quad (3.22)$$

$$\gamma_{Toep} = 2.237V_w \Omega_{turToep}^{-1} \quad (3.23)$$

$$T_t = T_{tur} / N_G, \quad \Omega_{tur} = \Omega_t / N_G, \quad (3.24)$$

where T_t and T_{tur} denote mechanical torques, and Ω_t and Ω_{tur} correspond to mechanical speeds, before and after the gearbox, respectively; N_G represents the gear ratio, and β indicates the pitch angle. Note in (3.23) and (3.24) that the mechanical speed is expressed as a Toeplitz-type matrix due to the harmonics produced by the DFIG and transmitted via the shaft.

3.4 Torsional shaft EHD model

The mechanical power transmission is constituted by the blades linked to the hub, coupled to the slow shaft, which is linked to the gearbox. The gearbox is used to match the rotational speed of the fast shaft connected to the generator.

In this thesis, a two-mass model is adopted to represent the fundamental frequency of the power transmission. Based on this idealized model, the mechanical dynamics in the EHD are described by (see Fig. 3.3 for reference directions)

$$\frac{d}{dt} \omega_t + D\omega_t = \frac{1}{J_t} [-(B_{tm} + B_t)\omega_t + B_{tm}\omega_m - K_{tm}\theta_t + K_{tm}\theta_m + PT_t], \quad (3.25)$$

$$\frac{d}{dt} \omega_m + D\omega_m = \frac{1}{J} [B_{tm}\omega_t - (B_{tm} + B_m)\omega_m + K_{tm}\theta_t - K_{tm}\theta_m + PT_e], \quad (3.26)$$

$$\Omega_t = \omega_t / P, \quad \Omega_m = \omega_m / P \quad (3.27)$$

where subscripts t and m refer to the turbine and machine side, respectively; ω_t and ω_m are the rotational speeds, whereas θ_t and θ_m denote the corresponding angle displacements, both in the EHD; J_t and J correspond to the turbine and machine inertia, respectively; K_m is the shaft spring constant; B_{tm} represents the mutual damping coefficient, and B_t and B_m indicate the self-damping coefficients, Fig. 3.3.

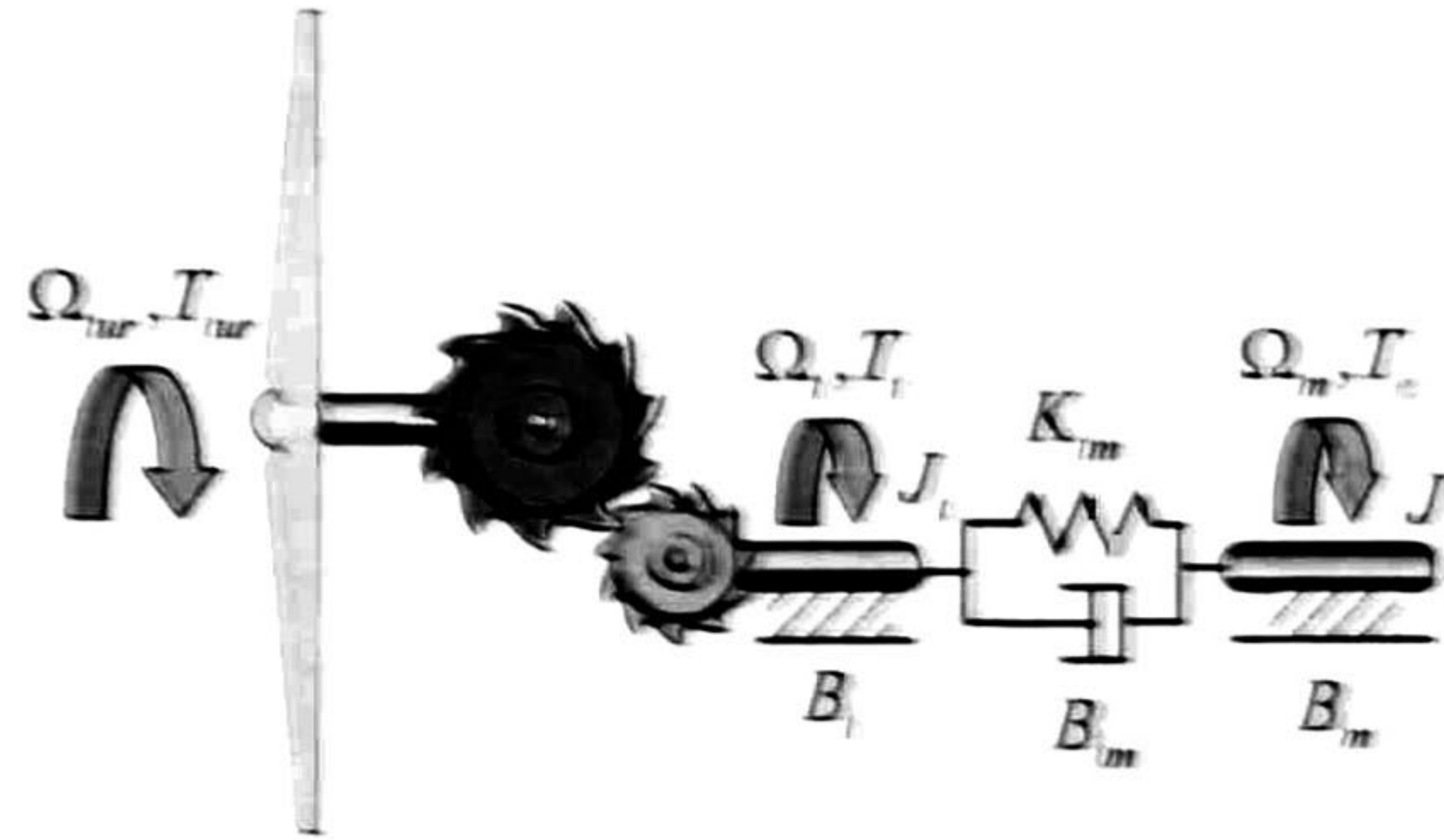


Fig. 3.3. Aerodynamic and two-mass representations.

3.4.1 Mechanical modes

Traditionally, the model given by (3.25) and (3.26) is simplified by neglecting the damping coefficients [11], resulting in a model with two inertias and the shaft spring. The resulting mechanical modes are given by

$$\omega_{1,2} = \pm \sqrt{-K_m \left(\frac{1}{J} + \frac{1}{J_t} \right)}. \quad (3.28)$$

For WTG around the MW capacity, the poles have a frequency in the range between 1 and 2 Hz [11].

3.5 BTB and RL Filter EHD models

Aimed to control power flow from the AC grid into the machine and vice-versa, a BTB converter, Fig. 3.4, is coupled to the DFIG via rotor terminals. Also, to diminish waveform distortion into the AC grid, an RL filter is included at the BTB converter grid-side terminals.

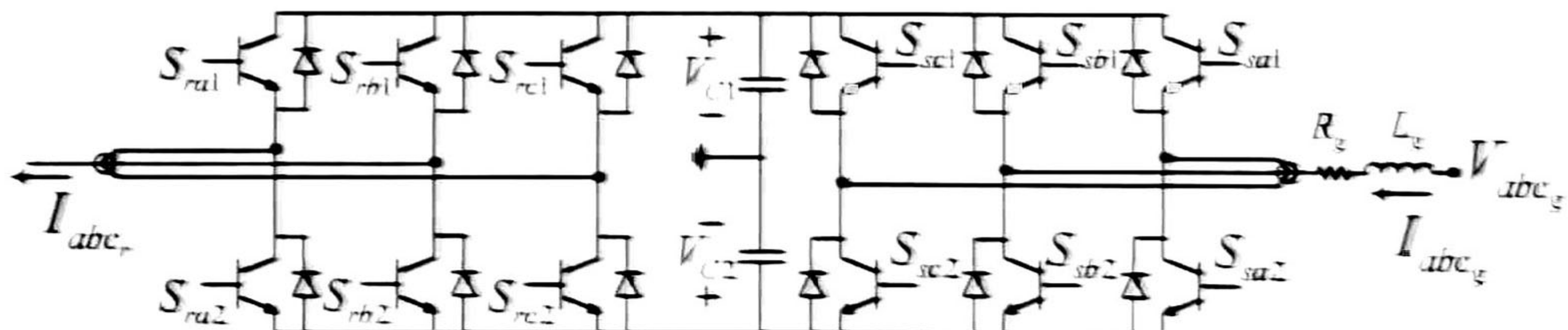


Fig. 3.4. BTB and RL Filter representation.

Based on the reference directions shown in Fig. 3.4, the BTB and RL filter EHD models are respectively given by

$$\frac{d}{dt} \begin{bmatrix} I_{ag} \\ I_{bg} \\ I_{cg} \end{bmatrix} + D \begin{bmatrix} I_{ag} \\ I_{bg} \\ I_{cg} \end{bmatrix} = -\frac{R_g}{L_g} \begin{bmatrix} I_{ag} \\ I_{bg} \\ I_{cg} \end{bmatrix} - \begin{bmatrix} \frac{S_{sa1}}{L_g} & \frac{S_{sa2}}{L_g} \\ \frac{S_{sb1}}{L_g} & \frac{S_{sb2}}{L_g} \\ \frac{S_{sc1}}{L_g} & \frac{S_{sc2}}{L_g} \end{bmatrix} \begin{bmatrix} V_{C1} \\ V_{C2} \end{bmatrix} + \frac{1}{L_g} \begin{bmatrix} V_{ag} \\ V_{bg} \\ V_{cg} \end{bmatrix}, \quad (3.29)$$

$$\frac{d}{dt} \begin{bmatrix} V_{C1} \\ V_{C2} \end{bmatrix} + D \begin{bmatrix} V_{C1} \\ V_{C2} \end{bmatrix} = \begin{bmatrix} \frac{S_{sa1}}{C_1} & \frac{S_{sb1}}{C_1} & \frac{S_{sc1}}{C_1} \\ \frac{S_{sa2}}{C_2} & \frac{S_{sb2}}{C_2} & \frac{S_{sc2}}{C_2} \end{bmatrix} \begin{bmatrix} I_{ag} \\ I_{bg} \\ I_{cg} \end{bmatrix} - \begin{bmatrix} \frac{S_{ra1}}{C_1} & \frac{S_{rb1}}{C_1} & \frac{S_{rc1}}{C_1} \\ \frac{S_{ra2}}{C_2} & \frac{S_{rb2}}{C_2} & \frac{S_{rc2}}{C_2} \end{bmatrix} \begin{bmatrix} I_{ar} \\ I_{br} \\ I_{cr} \end{bmatrix}, \quad (3.30)$$

where subscript g is related to the currents entering the RL filter from the grid-side, and subscript r denotes the current entering the DFIG rotor terminals; V_{Cx} represents voltages at capacitors terminals (DC-link); S_x indicates an HD switching Toeplitz-type matrix. The switching function corresponds to a three-phase converter PWM scheme explained next.

3.5.1 PWM scheme

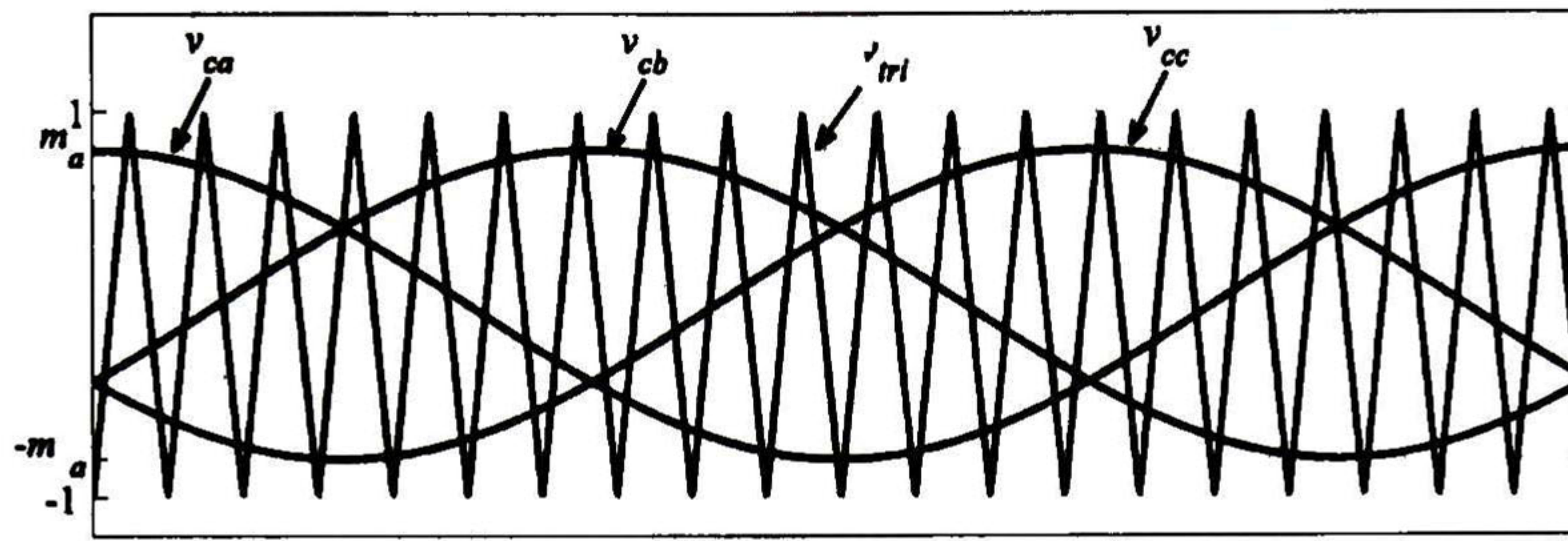
A three-phase converter can be obtained by connecting three single-phase converters in parallel; taking care of the 120° shifting between the control signals [26]. The PWM firing scheme relies on the comparison between a carrier signal (v_{tri}), commonly a triangular wave form signal, and control signals (v_{ca} , v_{cb} , and v_{cc}), as shown in Fig. 3.5. Hence, the corresponding switching actions are given by

$$\begin{aligned} v_{ca} > v_{tri} &\Rightarrow s_{a1} = 1 \text{ and } s_{a2} = 0, \\ v_{cb} > v_{tri} &\Rightarrow s_{b1} = 1 \text{ and } s_{b2} = 0, \\ v_{cc} > v_{tri} &\Rightarrow s_{c1} = 1 \text{ and } s_{c2} = 0. \end{aligned}$$

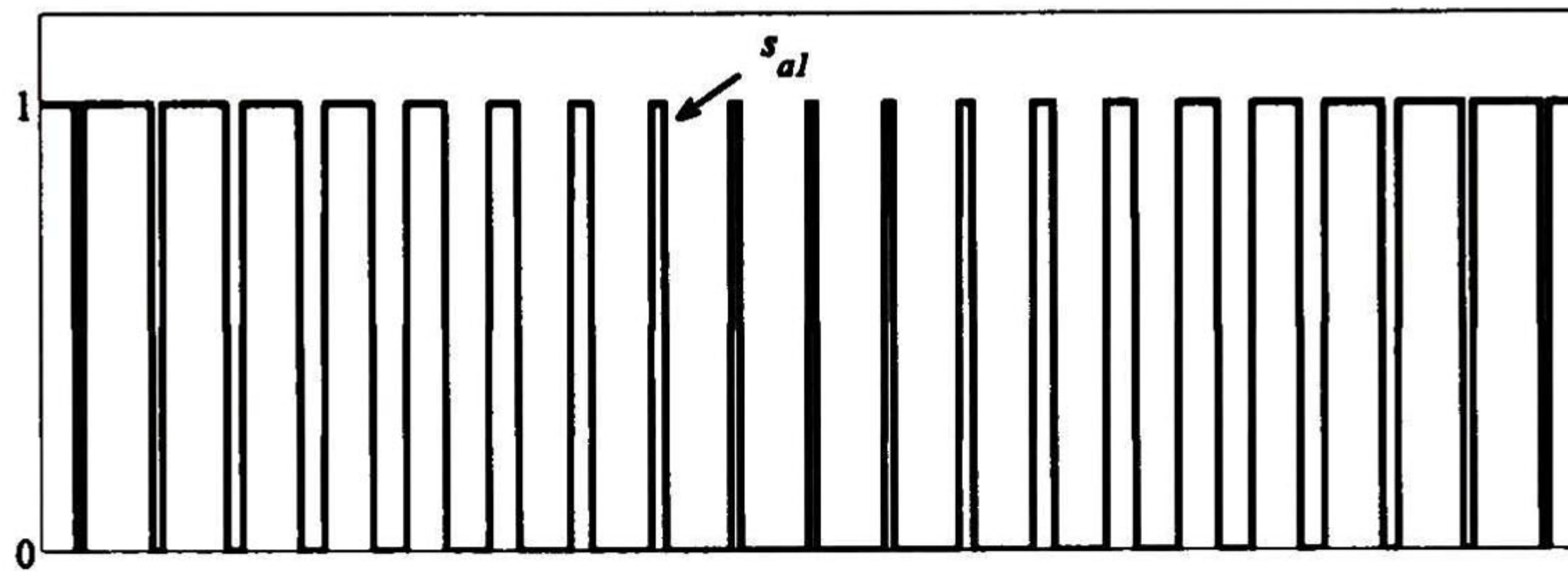
In Fig. 3.5, m_a is known as the modulation ratio corresponding to the amplitude of the control signals using a carrier signal of unitary amplitude; m_f denotes the frequency modulation ratio, given by

$$m_f = \frac{f_{sw}}{f_0},$$

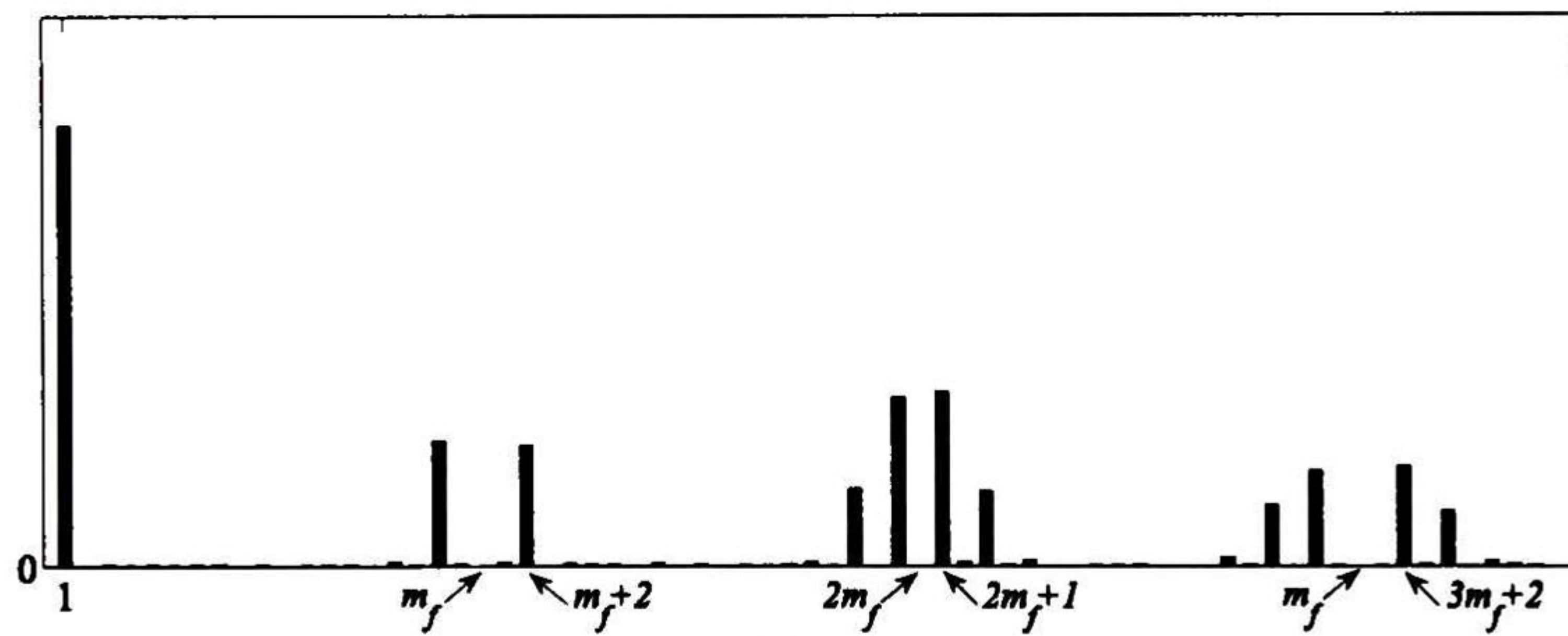
where f_{sw} represents the switching frequency, and f_0 denotes the fundamental frequency of the AC-system.



(a)



(b)



(c)

Fig. 3.5. Three-phase converter. a) Control and triangular signals. b) PWM scheme. c) Switching function spectrum.

Fig. 3.5(c) presents the harmonic spectrum of the converter switching functions; note that the “high-impact” harmonics are located around the switching frequency and its multiples.

The switching functions of the corresponding electronic switches consist of “zeros” and “ones”, as shown in Fig. 3.5(b). The harmonic content of a switching function is computed and expressed as a Toeplitz-type matrix S_x , and included into (3.29) or (3.30).

3.6 AC grid EHD model

For illustration purposes, the AC grid connected to the WTG is considered in this thesis as the one shown in Fig. 3.6. It consists of three overhead transmission lines, two loads, and one voltage source. The lines are considered as distributed-parameters frequency-dependent, represented by their frequency domain two-port admittance matrix:

$$Y = \begin{bmatrix} A & -B \\ -B & A \end{bmatrix}, \quad (3.31)$$

with:

$$A = Y_0 \coth(\gamma l),$$

$$B = Y_0 \operatorname{csch}(\gamma l),$$

where γ is the propagation function, Y_0 represents the characteristic admittance, and l denotes the line length.

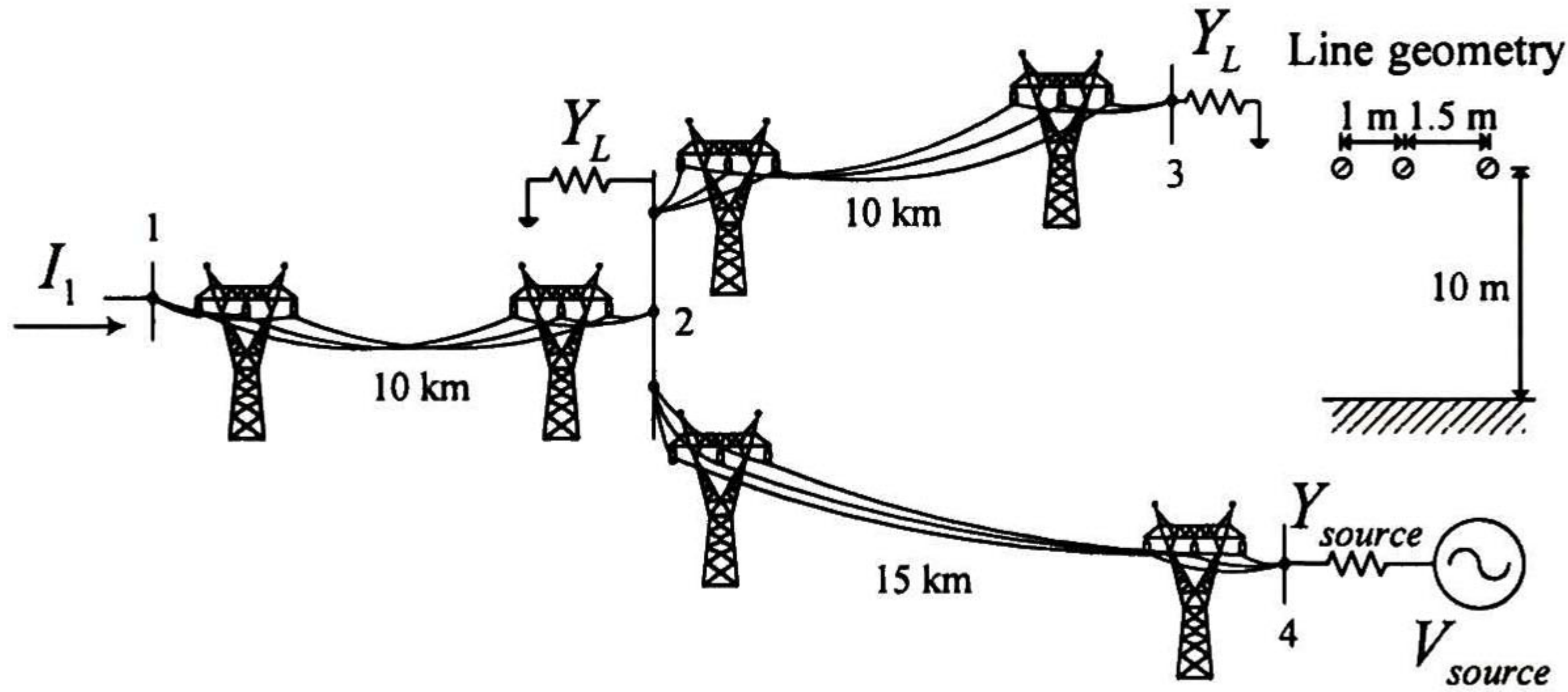


Fig. 3.6. AC grid connected to the DFIG and BTB converter.

The two-port input-admittance seen from nodes 1 and 4 of Fig. 3.6 is calculated and approximated by rational functions via the vector fitting (VF) software [27]-[30]. From the rational approximation given by VF, we obtain the EHD state-space system

$$\begin{aligned} \frac{d}{dt} X_{AC} + D X_{AC} &= A_{AC} X_{AC} + B_{AC} U_{AC} \\ V_{AC} &= C_{AC} X_{AC} + D_{AC} U_{AC} \end{aligned} \quad (3.32)$$

where:

$$V_{AC} = \begin{bmatrix} V_1 \\ V_4 \end{bmatrix}, \quad U_{AC} = \begin{bmatrix} I_1 \\ Y_{source} V_{source} \end{bmatrix}. \quad (3.33)$$

3.7 Assembling the EHD models

This section presents the complete WTG EHD system, separated in this thesis into electrical and mechanical subsystems due to the mechanical parts have slower dynamics than the electrical parts, resulting in faster simulation.

3.7.1 Electrical subsystem

The electrical subsystem is constituted by the DFIG, BTB converter, RL filter, and AC grid EHD models. The assembling of these models is described next.

Rewriting (3.16) gives

$$\frac{d}{dt} \begin{bmatrix} I_{\alpha_s} \\ I_{\beta_s} \\ I_{\alpha_r} \\ I_{\beta_r} \end{bmatrix} + D \begin{bmatrix} I_{\alpha_s} \\ I_{\beta_s} \\ I_{\alpha_r} \\ I_{\beta_r} \end{bmatrix} = \frac{1}{L_s L_r - L_m^2} \left(L_1 \begin{bmatrix} I_{\alpha_s} \\ I_{\beta_s} \\ I_{\alpha_r} \\ I_{\beta_r} \end{bmatrix} + L_{21} \begin{bmatrix} V_{\alpha_s} \\ V_{\beta_s} \end{bmatrix} + L_{22} \begin{bmatrix} V_{\alpha_r} \\ V_{\beta_r} \end{bmatrix} \right), \quad (3.34)$$

where:

$$L_{21} = \begin{bmatrix} L_r I & 0 \\ 0 & L_r I \\ -L_m I & 0 \\ 0 & -L_m I \end{bmatrix}, \quad L_{22} = \begin{bmatrix} -L_m I & 0 \\ 0 & -L_m I \\ L_s I & 0 \\ 0 & L_s I \end{bmatrix}.$$

Note that V_{α_r} and V_{β_r} depend on the voltage at the DC-link, and their relation is given by (see Appendix for definitions of transformation matrices)

$$\begin{bmatrix} V_{\alpha_r} \\ V_{\beta_r} \end{bmatrix} = MT_{DQ} \begin{bmatrix} S_{ra1} & S_{ra2} \\ S_{rb1} & S_{rb2} \\ S_{rc1} & S_{rc2} \end{bmatrix} \begin{bmatrix} V_{C1} \\ V_{C2} \end{bmatrix}. \quad (3.35)$$

Substituting (3.35) into (3.34) gives

$$\frac{d}{dt} \begin{bmatrix} I_{\alpha_s} \\ I_{\beta_s} \\ I_{\alpha_r} \\ I_{\beta_r} \end{bmatrix} + D \begin{bmatrix} I_{\alpha_s} \\ I_{\beta_s} \\ I_{\alpha_r} \\ I_{\beta_r} \end{bmatrix} = \frac{1}{L_s L_r - L_m^2} \left(L_1 \begin{bmatrix} I_{\alpha_s} \\ I_{\beta_s} \\ I_{\alpha_r} \\ I_{\beta_r} \end{bmatrix} + L_{21} \begin{bmatrix} V_{\alpha_s} \\ V_{\beta_s} \end{bmatrix} + L_{22} MT_{DQ} \begin{bmatrix} S_{ra1} & S_{ra2} \\ S_{rb1} & S_{rb2} \\ S_{rc1} & S_{rc2} \end{bmatrix} \begin{bmatrix} V_{C1} \\ V_{C2} \end{bmatrix} \right). \quad (3.36)$$

Transforming (3.29) and (3.30) to the stator reference frame, the $\alpha\beta$ -models of the BTB and the RL filter are respectively given by

$$\frac{d}{dt} \begin{bmatrix} I_{\alpha_g} \\ I_{\beta_g} \end{bmatrix} + D \begin{bmatrix} I_{\alpha_g} \\ I_{\beta_g} \end{bmatrix} = -\frac{R_g}{L_g} \begin{bmatrix} I_{\alpha_g} \\ I_{\beta_g} \end{bmatrix} - T_{\alpha\beta} \begin{bmatrix} \frac{S_{sa1}}{L_g} & \frac{S_{sa2}}{L_g} \\ \frac{S_{sb1}}{L_g} & \frac{S_{sb2}}{L_g} \\ \frac{S_{sc1}}{L_g} & \frac{S_{sc2}}{L_g} \end{bmatrix} \begin{bmatrix} V_{C1} \\ V_{C2} \end{bmatrix} + \frac{1}{L_g} \begin{bmatrix} V_{\alpha_s} \\ V_{\beta_s} \end{bmatrix}, \quad (3.37)$$

$$\frac{d}{dt} \begin{bmatrix} V_{C1} \\ V_{C2} \end{bmatrix} + D \begin{bmatrix} V_{C1} \\ V_{C2} \end{bmatrix} = \begin{bmatrix} \frac{S_{sa1}}{C_1} & \frac{S_{sb1}}{C_1} & \frac{S_{sc1}}{C_1} \\ \frac{S_{sa2}}{C_2} & \frac{S_{sb2}}{C_2} & \frac{S_{sc2}}{C_2} \end{bmatrix} T_{\alpha\beta}^{-1} \begin{bmatrix} I_{\alpha_g} \\ I_{\beta_g} \end{bmatrix} - \begin{bmatrix} \frac{S_{ra1}}{C_1} & \frac{S_{rb1}}{C_1} & \frac{S_{rc1}}{C_1} \\ \frac{S_{ra2}}{C_2} & \frac{S_{rb2}}{C_2} & \frac{S_{rc2}}{C_2} \end{bmatrix} T_{DQ}^{-1} M^{-1} \begin{bmatrix} I_{\alpha_r} \\ I_{\beta_r} \end{bmatrix}. \quad (3.38)$$

The electrical subsystem EHD model is assembled with (3.36) to (3.38). Despite of having dimensions larger than their corresponding instantaneous variable representations, the complete EHD model can be simplified due to the dependency that exists in the stator reference frame, noting the following:

1. The amplitudes of the generic variables (voltage, current, or flux) in the $\alpha\beta$ -reference frame, x_α and x_β , are equal to their abc -coordinates image amplitudes x_a , x_b , and x_c in a balanced system.
2. x_α and x_β are 90° phase shifted, $x_\beta = E x_\alpha$, where:

$$E = \text{diag} \left\{ e^{\frac{\pi}{2}j} \quad \dots \quad e^{\frac{\pi}{2}j} \quad 1 \quad e^{-\frac{\pi}{2}j} \quad \dots \quad e^{-\frac{\pi}{2}j} \right\}$$

3. x_α in EHD has double information data (magnitude and phase).
4. As a result of having a balanced system, $V_{C2} = -V_{C1}$, is satisfied.

Based on the aforementioned four items, the simplified electrical subsystem model is given by

$$\boxed{\frac{d}{dt} \begin{bmatrix} I_{\alpha_s} \\ I_{\alpha_r} \\ I_{\alpha_g} \\ V_{C1} \end{bmatrix} + D \begin{bmatrix} I_{\alpha_s} \\ I_{\alpha_r} \\ I_{\alpha_g} \\ V_{C1} \end{bmatrix} = \begin{bmatrix} A_1 & 0 & A_2 \\ 0 & A_3 & A_4 \\ 0 & A_5 & A_6 & 0 \end{bmatrix} \begin{bmatrix} I_{\alpha_s} \\ I_{\alpha_r} \\ I_{\alpha_g} \\ V_{C1} \end{bmatrix} + \begin{bmatrix} A_7 \\ A_8 \\ 0 \end{bmatrix} V_{\alpha_s}}, \quad (3.39)$$

where the elements A_1 to A_8 are given by

$$A_1 = \frac{1}{L_s L_r - L_m^2} \begin{bmatrix} -r_s L_r I + \omega_{m_{\text{roep}}} L_m^2 E & r_r L_m I + \omega_{m_{\text{roep}}} L_m L_r E \\ r_s L_m I - \omega_{m_{\text{roep}}} L_m L_s E & -r_r L_s I - \omega_{m_{\text{roep}}} L_s L_r E \end{bmatrix},$$

$$A_2 = \frac{1}{L_s L_r - L_m^2} \begin{bmatrix} -L_m I & 0 \\ L_s I & 0 \end{bmatrix} MT_{DQ} \begin{bmatrix} S_{ra1} - S_{ra2} \\ S_{rb1} - S_{rb2} \\ S_{rc1} - S_{rc2} \end{bmatrix},$$

$$A_3 = -(R_g / L_g) I.$$

$$A_4 = \frac{2}{3} \begin{bmatrix} I & -\frac{1}{2} I & -\frac{1}{2} I \end{bmatrix} \begin{bmatrix} -\frac{S_{sa1}}{L_g} + \frac{S_{sa2}}{L_g} \\ -\frac{S_{sb1}}{L_g} + \frac{S_{sb2}}{L_g} \\ -\frac{S_{sc1}}{L_g} + \frac{S_{sc2}}{L_g} \end{bmatrix},$$

$$A_5 = \begin{bmatrix} -\frac{S_{ra1}}{C_1} (I \cos \theta_m + \sin \theta_m E) \\ -\frac{S_{rb1}}{C_1} \left(\left(-\frac{1}{2} I \cos \theta_m - \frac{\sqrt{3}}{2} I \sin \theta_m \right) + \left(-\frac{1}{2} \sin \theta_m + \frac{\sqrt{3}}{2} \cos \theta_m \right) E \right) \\ -\frac{S_{rc1}}{C_1} \left(\left(-\frac{1}{2} I \cos \theta_m + \frac{\sqrt{3}}{2} I \sin \theta_m \right) + \left(-\frac{1}{2} \sin \theta_m - \frac{\sqrt{3}}{2} \cos \theta_m \right) E \right) \end{bmatrix},$$

$$A_6 = \begin{bmatrix} \frac{S_{sa1}}{C_1} & \frac{S_{sb1}}{C_1} & \frac{S_{sc1}}{C_1} \end{bmatrix} \begin{bmatrix} I \\ -\frac{1}{2} I + \frac{\sqrt{3}}{2} E \\ -\frac{1}{2} I - \frac{\sqrt{3}}{2} E \end{bmatrix},$$

$$A_7 = \frac{1}{L_s L_r - L_m^2} \begin{bmatrix} L_r I \\ -L_m I \end{bmatrix},$$

$$A_8 = (1 / L_g) I$$

Also, the interface between the AC grid and the WTG is given by (see Fig. 3.4 and Fig. 3.6 for reference directions)

$$\begin{bmatrix} V_{\alpha_s} \\ V_{\beta_s} \end{bmatrix} = \frac{1}{K_T} T_{\alpha\beta} V_1, \quad (3.40)$$

$$U_{AC} = \begin{bmatrix} I_1 \\ Y_{source} V_{source} \end{bmatrix} = \begin{bmatrix} -\frac{1}{K_T} T_{\alpha\beta}^{-1} \left(\begin{bmatrix} I_{\alpha_s} \\ I_{\beta_s} \end{bmatrix} + \begin{bmatrix} I_{\alpha_g} \\ I_{\beta_g} \end{bmatrix} \right) \\ Y_{source} T_{\alpha\beta}^{-1} \begin{bmatrix} V_{\alpha_{source}} \\ V_{\beta_{source}} \end{bmatrix} \end{bmatrix}, \quad (3.41)$$

where K_T corresponds to the transformer ratio.

3.7.2 Mechanical subsystem

The mechanical subsystem involves the aerodynamic and the torsional shaft EHD models, given in (3.25) and (3.26) and, for convenience, repeated here as

$$\frac{d}{dt} \omega_t + D\omega_t = \frac{1}{J_t} [-(B_{tm} + B_t)\omega_t + B_{tm}\omega_m - K_{tm}\theta_t + K_{tm}\theta_m + PT_t], \quad (3.42)$$

$$\frac{d}{dt} \omega_m + D\omega_m = \frac{1}{J} [B_{tm}\omega_t - (B_{tm} + B_m)\omega_m + K_{tm}\theta_t - K_{tm}\theta_m + PT_e], \quad (3.43)$$

where:

$$T_t = \frac{\rho\pi R^3 V_w^2 C_p \lambda^{-1}}{2N_G}. \quad (3.44)$$

$$T_e = \frac{3}{2} L_m P \begin{bmatrix} I_{\beta_{SToeP}} & -I_{\alpha_{SToeP}} \end{bmatrix} \begin{bmatrix} I_{\alpha_r} \\ I_{\beta_r} \end{bmatrix}. \quad (3.45)$$

3.8 Control scheme

The main objectives in controlling a WTG are to improve its performance and to achieve quality of power conversion, ensuring additionally that the generator is within a safe operating region [15].

The WTG operation is divided into two regions, Fig. 3.7: a) region 1, in which the control maximizes the energy captured from the wind, and b) region 2, in which the control limits the generated power below its rate value to avoid damage [15]. Therefore, the scheme control is divided into low- and high-level [15], Fig. 3.8, to achieve the

aforementioned control objectives. Both levels are only briefly described because this topic is beyond the scope of this thesis.

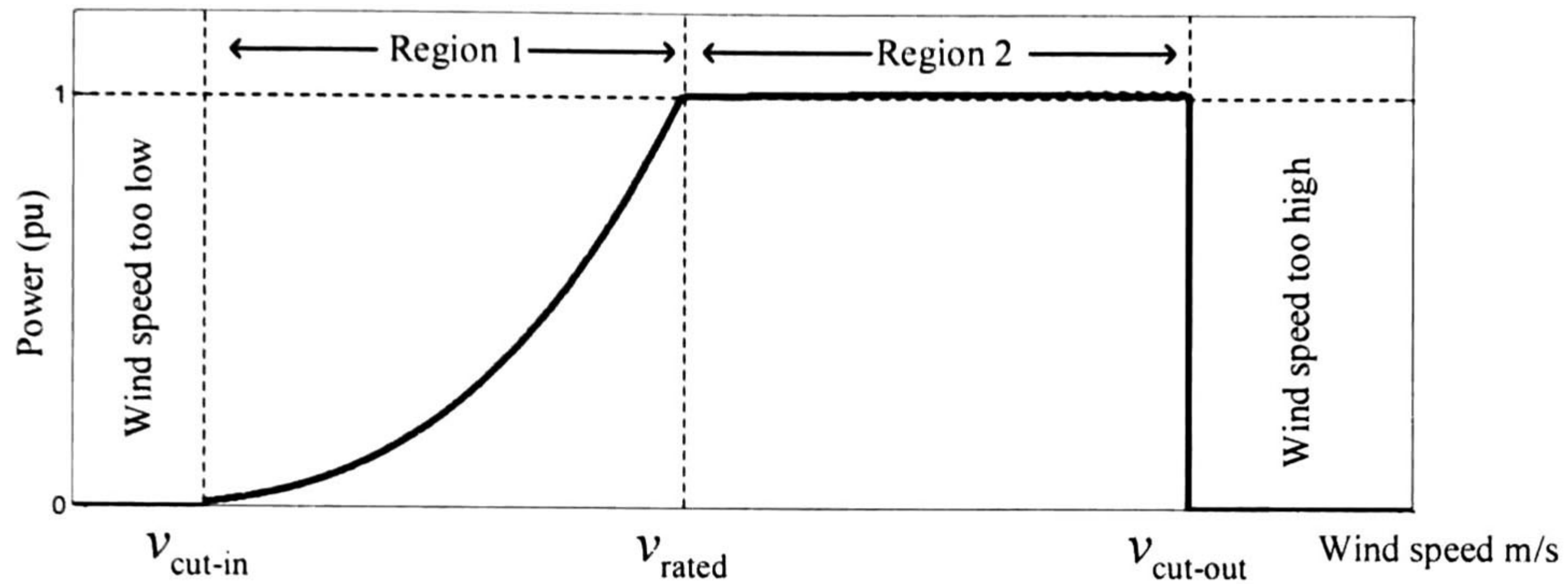


Fig. 3.7. Operation regions of the WTG.

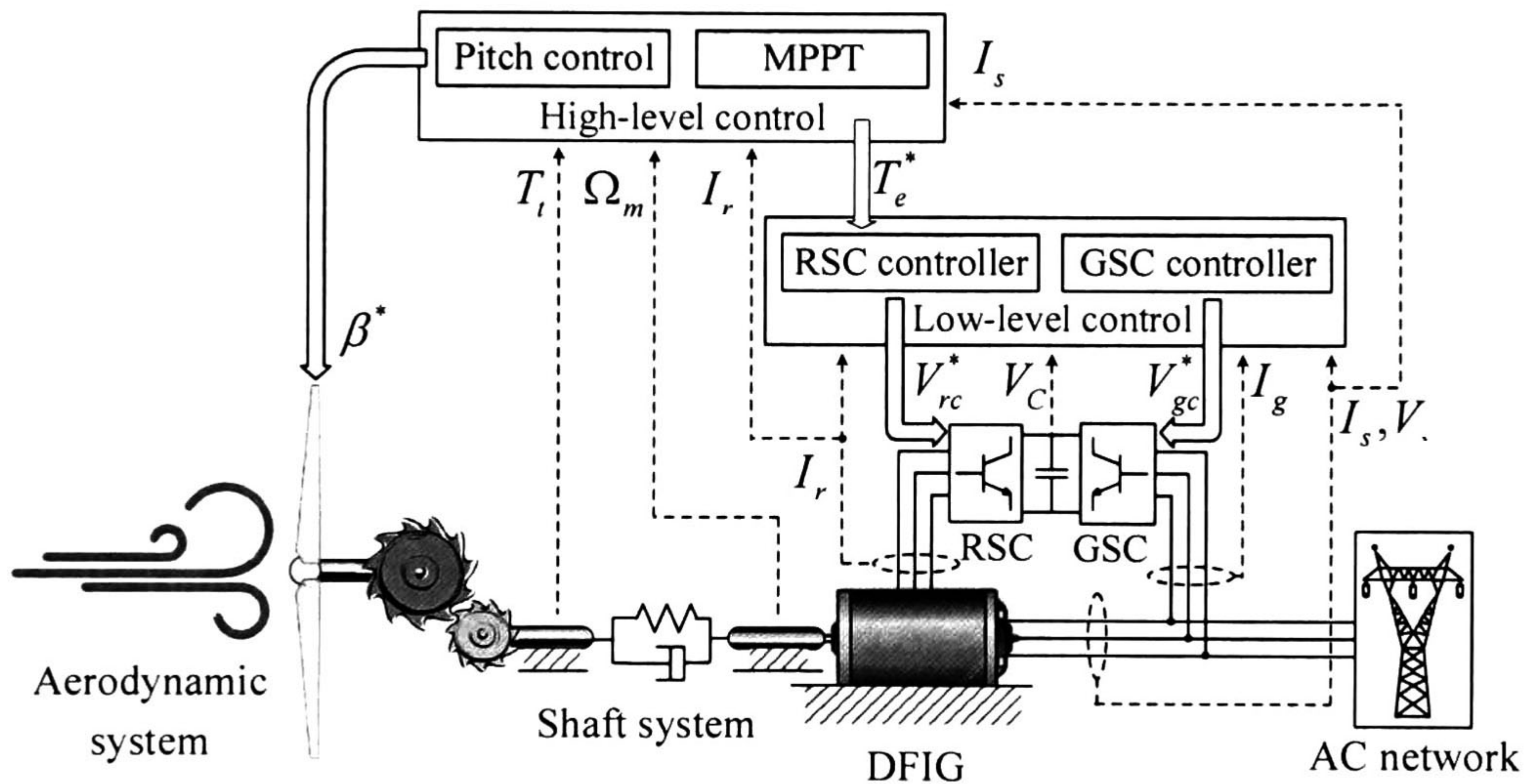


Fig. 3.8. Control scheme of the WTG system.

For simplicity of exposition, PI controls are used in this thesis. Nevertheless, other types of control schemes, e.g., sliding-mode or fuzzy-based, can be adopted due to EHD flexibility for readily converting between time and harmonic domain quantities.

3.8.1 Low-level control

Traditionally, the low-level control of a WTG system is simplified by representing the BTB converter as controllable voltage sources at fundamental frequency [13]-[18]. In this thesis, the low-level control is performed via a pure-sine PWM (PS-PWM) scheme. Harmonics in the BTB model are accounted for, resulting in more accurate results than those by existing models.

The low-level control is subdivided into two decoupled controls, Fig. 3.8: a) rotor-side converter (RSC) control, and b) grid-side converter (GSC) control. Also, the low-level control scheme provides the magnitudes and phases, $|V_{rc}|$, $|V_{gc}|$, φ_{rc} , and φ_{gc} , corresponding to sinusoidal-type references for the RSC and GSC, respectively, Fig. 3.8. These parameters are achieved by means of control actions which are described next.

3.8.1.1 Rotor-side converter (RSC) control

The objective of the RSC control is to regulate both the DFIG electromagnetic torque and the stator reactive power. The electromagnetic control relies on (3.15). Considering fundamental frequency for control purposes only, we obtain from (3.15)

$$|i_{\alpha_r}^*| = \frac{2T_e^*}{3L_m P |i_{\alpha_s}| \sin(\varphi_s - \varphi_r)} \quad (3.46)$$

The control of the stator reactive power, given by (3.47), relies on the power factor (PF) reference.

$$Q_s^* = \sqrt{\left(\frac{P_m}{PF^*}\right)^2 - P_m^2} \quad (3.47)$$

In (3.46) and (3.47), superscript “*” denotes reference values, P_m is the mechanical power, and φ_s and φ_r correspond to phases of stator and rotor currents, respectively. Based on (3.46) and (3.47), the block diagrams of the RSC control are depicted in Fig. 3.9.

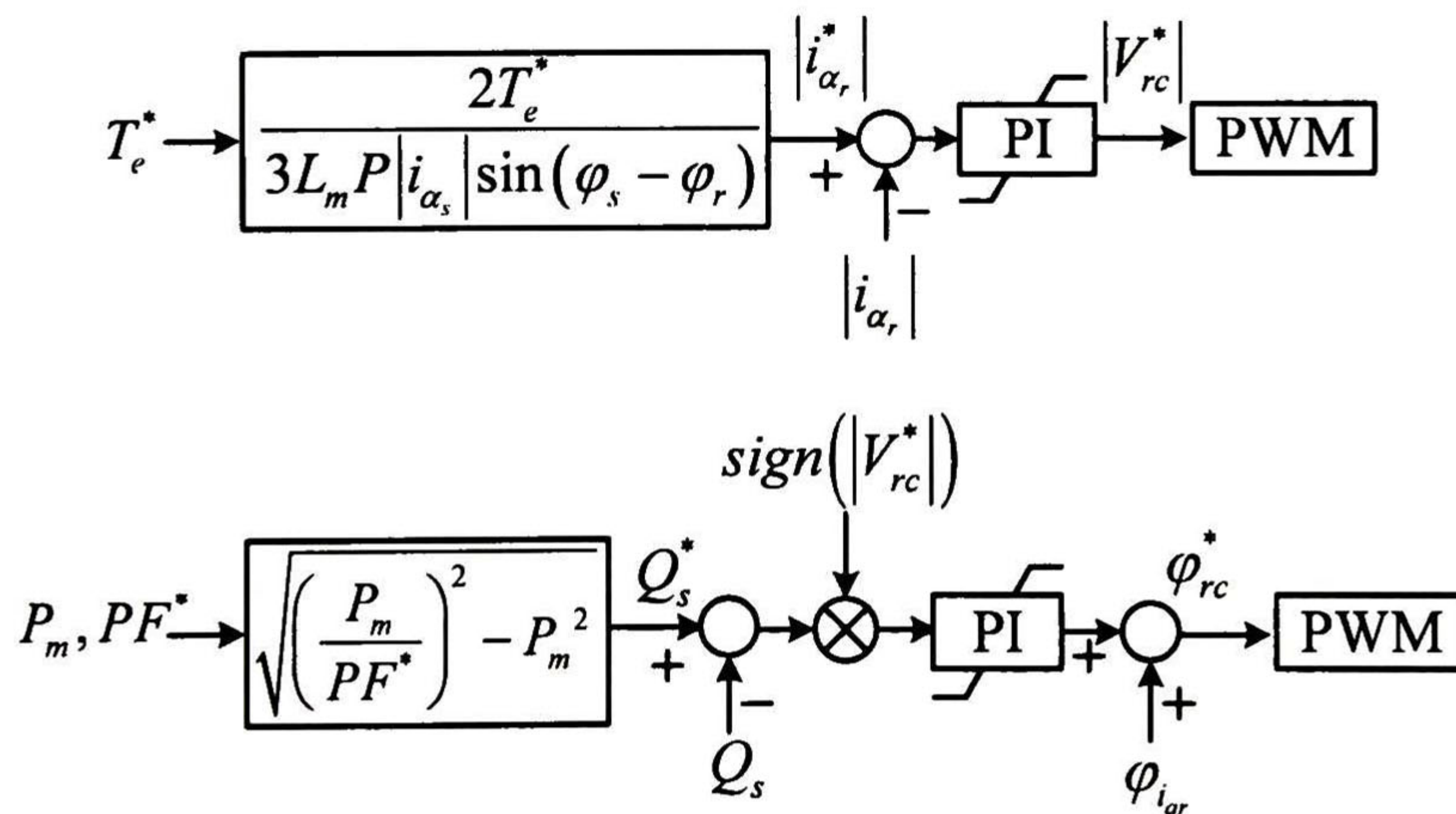


Fig. 3.9. Block diagrams of the RSC control loop.

3.8.1.2 Grid-side converter (GSC) control

The objective of the GSC control is to maintain a constant voltage at the DC-link. A cascade control structure is implemented in the proposed EHD model, where the primary controller consists in regulating the grid-side currents, whereas the secondary controller is responsible for regulating the squared DC voltage. The active power in the DC-link is given by

$$P_{DC} = \frac{3}{2} (i_{\alpha_g} v_{\alpha_s} + i_{\beta_g} v_{\beta_s}). \quad (3.48)$$

From (3.48), and considering fundamental frequency for control purposes only, gives

$$|i_{\alpha_g}^*| = \frac{2P_{DC}^*}{3|v_{\alpha_s}| \cos(\varphi_v - \varphi_g)} \quad (3.49)$$

Based on (3.49), the block diagram of the GSC is depicted in Fig. 3.10, where φ_v and φ_g represent grid-side voltage and current angles, respectively, and v_C corresponds to the voltage at the DC-link.

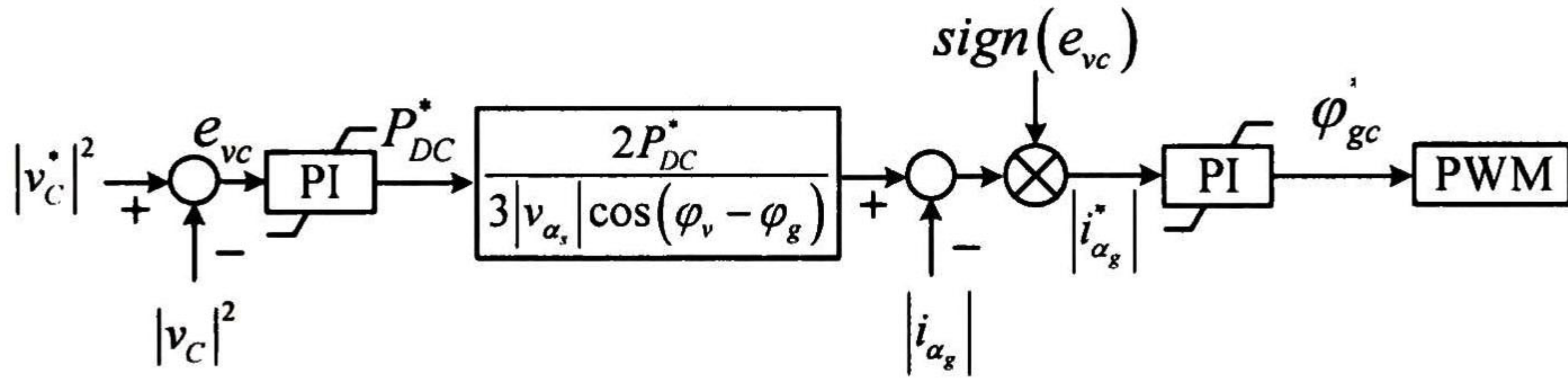


Fig. 3.10. Block diagram of the GSC control loop.

3.8.2 High-level control

The high-level control objective is aimed to ensure the maximum energy conversion by means of an optimum speed; also, it sets the electromagnetic torque reference for the low-level control, Fig. 3.8.

3.8.2.1 Pitch control

The pitch control is responsible for extracting the excess of energy from the wind. In other words, if the WTG is operating in region 2, Fig. 3.7, the pitch control is activated to keep the extracting power at its nominal value. The pitch actuator consists of a nonlinear servo which can be modeled in closed-loop as a first-order dynamic system with saturation in the pitch angle (β) [5], [15], Fig. 3.11. Typically, β varies at a maximum rate of 10 °/s in a range from 0° to 30° [5], [15].

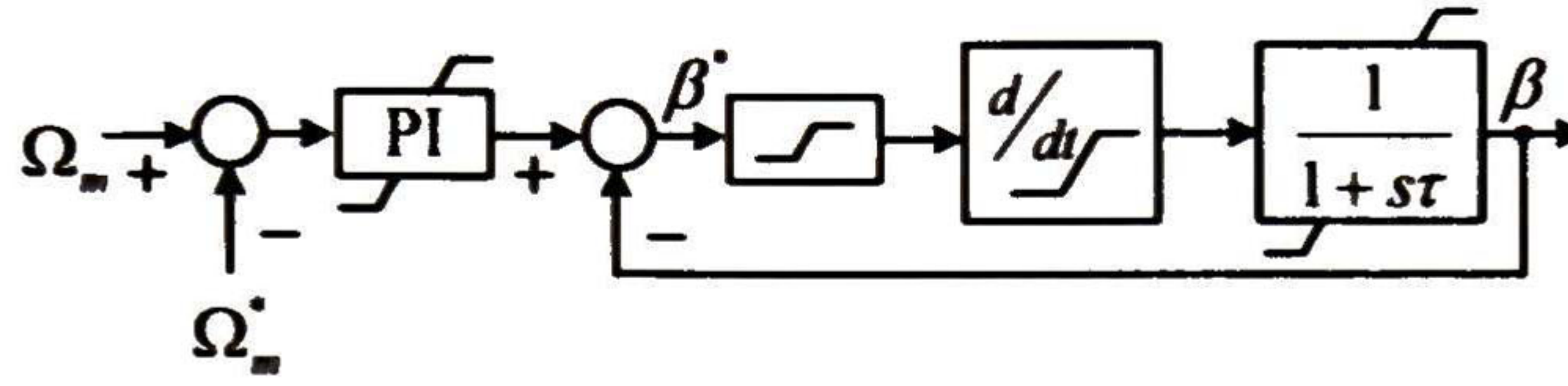


Fig. 3.11. Block diagram of the pitch control.

In Fig. 3.11, Ω_m^* represents the mechanical speed reference of the machine, defined by

$$\Omega_m^* = \Omega_m + K_\Omega (1 - \hat{P}_m), \quad (3.50)$$

where \hat{P}_m corresponds to the mechanical power in pu, and K_Ω denotes a constant value.

3.8.2.2 Maximum power point tracking (MPPT)

The maximum energy conversion in a WTG system is achieved at the optimum speed via a maximum power point tracking (MPPT) algorithm. The MPPT algorithms used in practice are: 1) torque reference-based, 2) searching-based, and 3) fuzzy-based [2].

In this thesis, the searching-based MPPT algorithm, also known as the perturbation and observation (P&O) method [2], is adopted due to its simplicity and good performance.

The main purpose of an MPPT algorithm is to maintain the WTG operating point around the maximum power coefficient $C_{P_{\max}}$ for any wind speed, Fig. 3.12. The operating points can be either on the positive slope (left of $C_{P_{\max}}$), at the zero slope (at $C_{P_{\max}}$), and on the negative slope (right of $C_{P_{\max}}$), Fig. 3.12. The P&O method relies on the following principle. If an operating point is on the positive slope region, the controller will move to the right towards the optimum speed. This can be achieved by decreasing the magnitude of the electromagnetic torque which results in an increase of the rotational speed. Conversely, if the operating point lies on the negative slope region, the magnitude of the electromagnetic torque has to be increased, resulting in a decrease of the rotational speed.

The control flowchart of the P&O method, shown in Fig. 3.13, illustrates the details of the decision process. If the rotational speed is higher than the cut-in speed, the MPPT controller will start the P&O procedure at sequential steps until reaching the optimum speed.

In Fig. 3.13, m_{\max} is a constant that represents the slope when the point is far from $C_{P_{\max}}$, *limit* represents a constant that allows increasing or decreasing rotational speed faster because of the large distance between the current point and $C_{P_{\max}}$. It is noted that, when the point is close to $C_{P_{\max}}$, m is close to zero; hence, $T_e^* \cong -T_t$; the machine achieves the optimum speed and there is no acceleration.

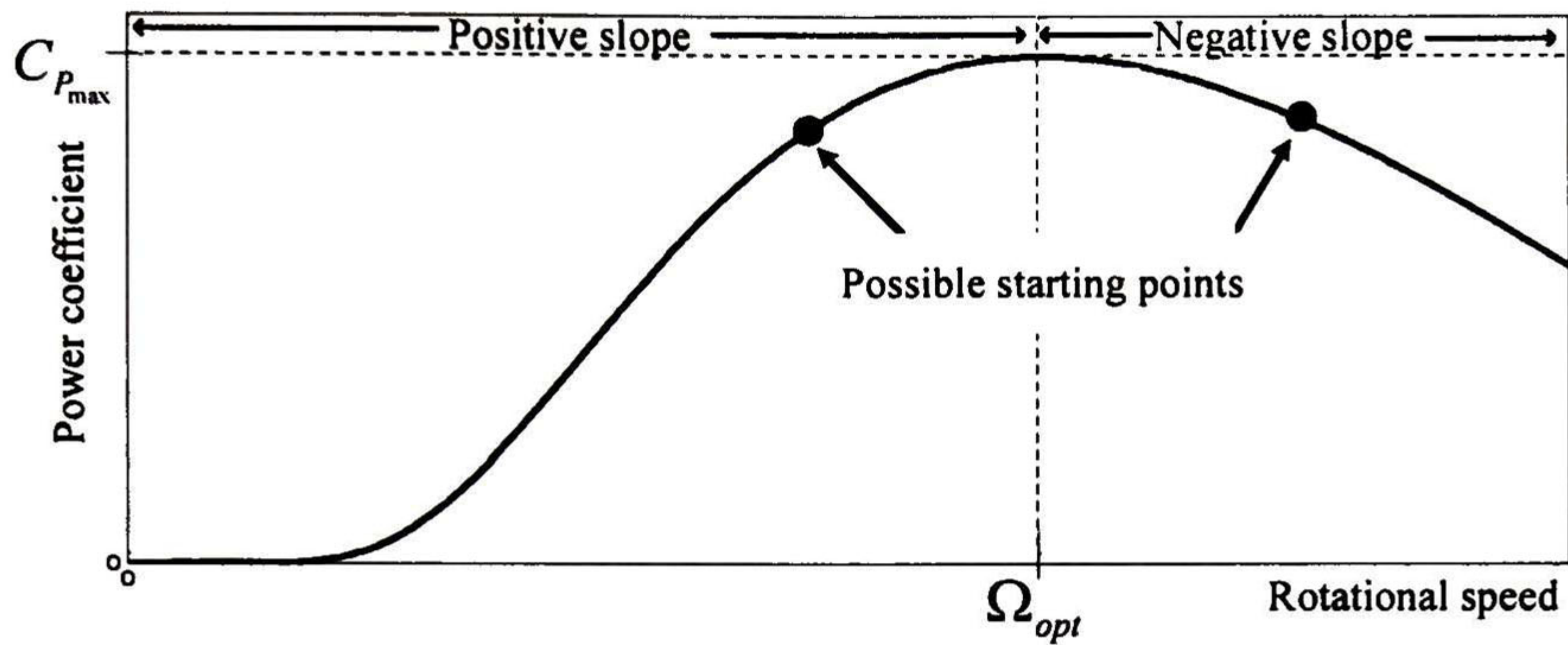


Fig. 3.12. Power with MPPT process.

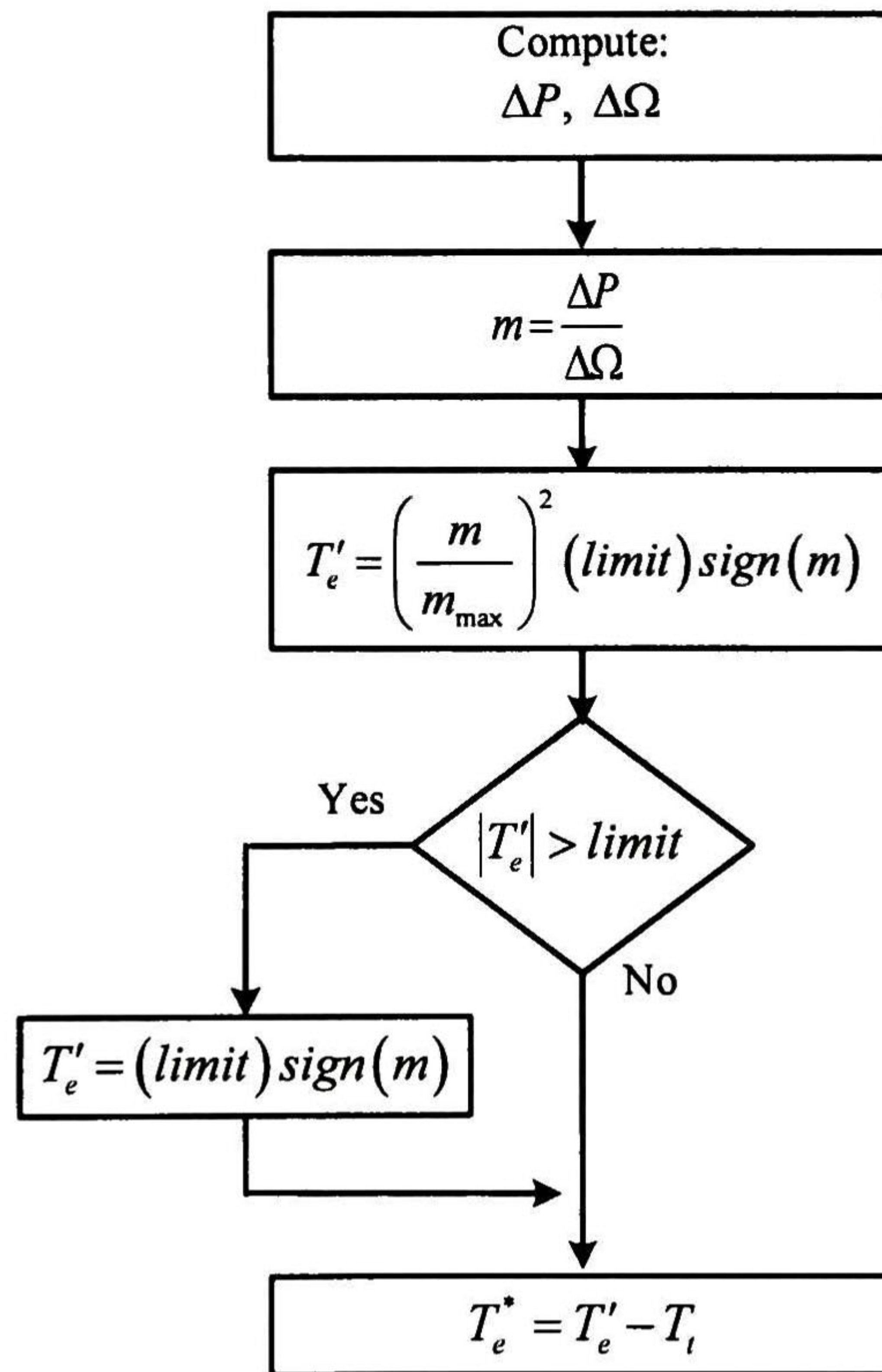


Fig. 3.13. Flowchart of MPPT.

3.9 High-impact harmonics

The proposed WTG EHD model is capable of accounting for an arbitrary number of harmonics; nevertheless, the more harmonics included the larger the space-state EHD system becomes. This affects the CPU by the transient simulation. To avoid large dimensions due to the presence of switching harmonics, this thesis addresses this issue by considering “high-impact” harmonics only.

The “high-impact” harmonics are selected based on the harmonic spectrum of the converter switching functions, as illustrated in Fig. 3.5(c). Based on the harmonic spectrum, only a) fundamental AC frequency and its neighbors, and b) switching frequency and its multiples with corresponding neighbors, are selected, Fig. 3.14. This results in compact EHD vectors.

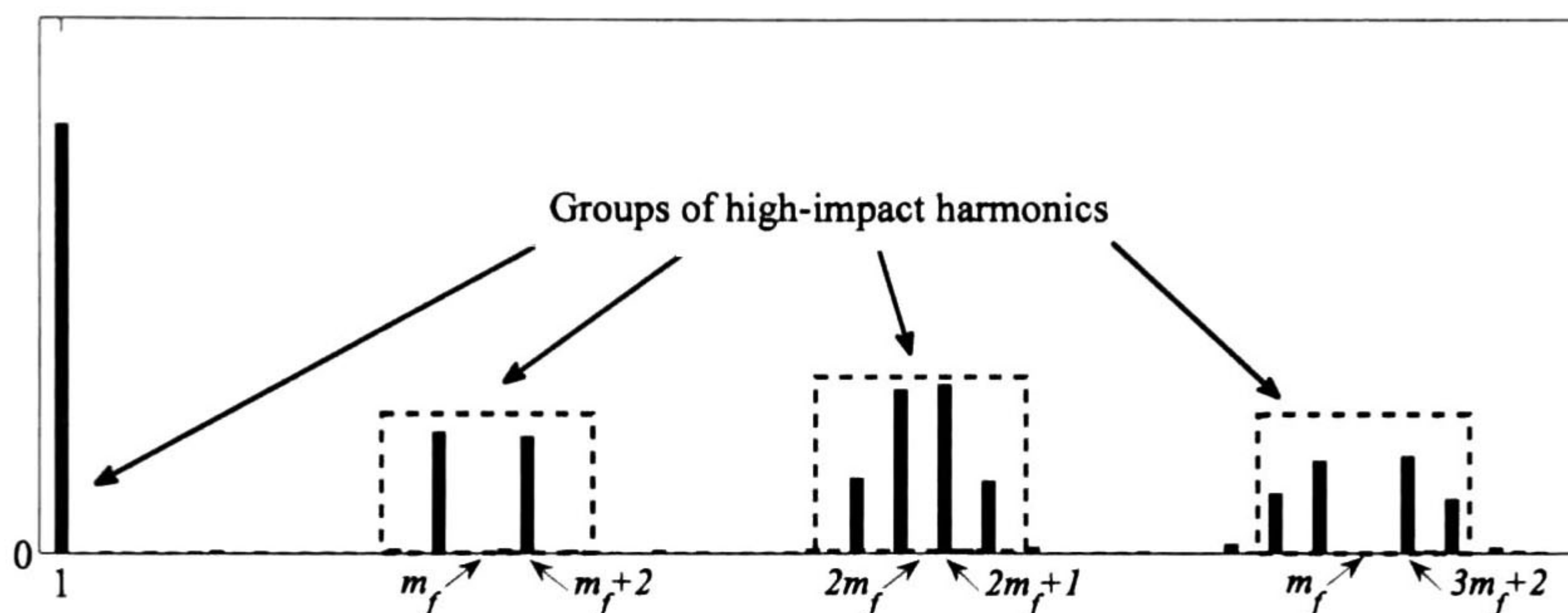


Fig. 3.14. High-impact harmonics in switching function spectrum.

3.10 WTG system solution

Based on the WTG EHD model and the control scheme outlined in this Chapter; the dynamic simulation of the WTG system of Fig. 3.8, considering “high-impact” harmonics only, can be performed by evaluating the next steps:

1. Select the “high-impact” harmonics under study based on the switching function frequency spectrum.
2. Compute the rational approximation of the AC grid.
3. Convert the rational approximation from step 2 into an EHD state-space system as in (3.32).
4. Set initial conditions for all variables of the WTG.
5. The dynamic solution starts here.
 - 5.1. Compute the switching functions by using the PWM scheme described in Section 3.5.1 and the current values of the sinusoidal-type references for the RSC and GSC ($|V_{rc}|$, $|V_{gc}|$, φ_{rc} , and φ_{gc}). Convert the switching functions into Toeplitz-type matrices.

- 5.2. Calculate M with the value of θ_m at time-step k (see Appendix for definition of M).
- 5.3. With the current values of the AC grid states compute the interface between the grid and the WTG using (3.32), (3.33), and (3.40).
- 5.4. Having in mind that (3.39) has been discretized by using the trapezoidal rule, calculate electrical state variables at time-step $k + 1$.
- 5.5. Update the AC grid states by using the electrical state variables at time-step $k + 1$ and the relations for the interface between the grid and the WTG, given by (3.32) and (3.41).
- 5.6. With the values of the electrical state variables at time-step $k + 1$ compute the electromagnetic torque defined by (3.45).
- 5.7. Using (3.44), compute the mechanical torque at the turbine side (T_l).
- 5.8. Using the Euler method in the discretization of (3.42) and (3.43) predict values for the rotational speeds.
- 5.9. Using the speeds predicted in step 5.8 and the angle displacements at time-step k , compute predicted angle displacements with

$$\begin{bmatrix} \theta_l \\ \theta_m \end{bmatrix}^{pred} = \begin{bmatrix} \theta_l \\ \theta_m \end{bmatrix}^k + \Delta t \begin{bmatrix} \omega_l \\ \omega_m \end{bmatrix}^k$$
- 5.10. Using the predicted values of the mechanical state variables compute a predicted mechanical torque by using (3.44).
- 5.11. With the predicted values of the mechanical variables computed above, calculate the rotational speeds at time-step $k + 1$ by applying the trapezoidal rule to (3.42) and (3.43).
- 5.12. Compute the corrected angular displacements at time-step $k + 1$ by using the relation:

$$\begin{bmatrix} \theta_l \\ \theta_m \end{bmatrix}^{k+1} = \begin{bmatrix} \theta_l \\ \theta_m \end{bmatrix}^k + \frac{\Delta t}{2} \left(\begin{bmatrix} \omega_l \\ \omega_m \end{bmatrix}^k + \begin{bmatrix} \omega_l \\ \omega_m \end{bmatrix}^{k+1} \right).$$
- 5.13. Update β by using the block diagram represented in Fig. 3.11.
- 5.14. Compute the new electromagnetic torque reference by means of the flowchart shown in Fig. 3.13.
- 5.15. Update the values of the sinusoidal-type references for RSC by using the block diagram depicted in Fig. 3.9.
- 5.16. By means of the block diagram shown in Fig. 3.10, the values of the sinusoidal-type references for GSC are updated.
6. Convert the data given in the EHD into the TD for visualization purposes.

3.11 Conclusions

The EHD models of the WTG elements, including both mechanical and electrical subsystems have been described in this Chapter. This thesis adopts the mechanical models corresponding to the available blocks of PSCAD/EMTDC in order to compare the results of the proposed WTG system with those by PSCAD/EMTDC.

The complete EHD model has been simplified by taking advantage of the dependency that exists in the stator reference frame for a balanced system, leading to a complete model using the α -coordinate only. As a result, a decreased CPU time is achieved due to the reduced dimensions of the system.

An efficient heuristic remedy which consists on accounting for “high-impact” harmonics only has been adopted, achieving further reduced dimensions of harmonic domain vectors and decreasing the CPU time by the transient simulation.

A major feature of the proposed model is the insertion of harmonics in mechanical systems, where vibrations can be attributed and expressed in terms of harmonics, produced by electrical variables in the DFIG and transmitted via the shaft system.

4 CASE STUDY

In this Chapter the proposed WTG EHD model and solution scheme are verified and validated via a case study. The proposed EHD model has been implemented in MatLab® and compared with the PSCAD/EMTDC software tool.

4.1 System description and data

A typical 2 MW WTG is adopted as part of the case study. The parameters of the simulated system are shown in Table 4.1.

Table 4.1. System data.

DFIG		
V_s	690 V, 50 Hz	Stator voltage (L-L)
r_s	2.6 m Ω	Stator resistance
r_r	2.9 m Ω	Rotor resistance (referred to stator)
L_{ls}	0.087 mH	Stator leakage inductance of stator
L_{lr}	0.087 mH	Rotor leakage inductance (referred to stator)
L_m	2.5 mH	Magnetizing inductance
P	2	Pole pairs
T_b	12,732 Nm	Rated torque
S_b	2 MW	Rated power
Ω_b	157.079 rad/s	Rated machine speed
J	90 kgm ²	Inertia of the machine
BTB and RL Filter		
f_{sw}	2 kHz	Switching frequency
f_0	50 Hz	Sinusoidal-type reference frequency
C	0.5 F	DC-link capacitors
R_{thyr}	0.0506 Ω	Thyristor resistance
R_g	0.05 Ω	Filter resistance
L_g	0.5 mH	Filter inductance
Aerodynamic model		
V_w	variable	Wind speed
β	variable	Pitch angle
R	31.5 m	Length of the blades
ρ	1.225 kg/m ³	Air density
N_G	90.5	Gear ratio
S_b	2 MW	Rated power

Torsional shaft model		
B_t	0 Nms/rad	Turbine self-damping
B_m	0 Nms/rad	Machine self-damping
B_{tm}	0 Nms/rad	Mutual damping
K_{tm}	10500 Nm/rad	Shaft spring constant
J_t	50 kgm ²	Inertia of the turbine
Transformer		
K_t	115 kV/0.69 kV	Transformer ratio
Source		
V_{source}	115 kV, 50 Hz	Voltage (L-L)
Y_{source}	5 m Ω	Source resistance
Grid		
r_c	0.03206 Ω /km	Conductor DC resistance
ρ_m	100 Ω m	Ground resistivity
Φ_c	3.2 cm	Conductor diameter
Y_L	100 Ω	Load
N	9	Set of poles
Pitch control		
τ	0.2 s	Actuator time constant
K_I	2	Integral gain
K_P	0.75	Proportional gain
K_Ω	1.3812	Proportional constant
RSC Controller		
K_I	0.01	Integral gain (torque control)
K_P	0.00005	Proportional gain (torque control)
K_I	0.0002	Integral gain (reactive power control)
K_P	0.000001	Proportional gain (reactive power control)
PF^*	0.98	Power factor reference
GSC Controller		
$ V_{gc} $	0.9	Magnitude of the sinusoidal-type reference
K_I	0.1	Integral gain (voltage control)
K_P	0.01	Proportional gain (voltage control)
K_I	0.5	Integral gain (current control)
K_P	0.01	Proportional gain (current control)
V_C^*	600 V	DC-link voltage reference
MPPT algorithm		
$limit$	0.2	Constant of slope
m_{max}	20000	Constant of increase

4.2 Numerical results

Fig. 4.1 to Fig. 4.6 present the main variables of the WTG system obtained with both the proposed EHD model and PSCAD/EMTDC. For this case study, an arbitrary wind-speed ranging from 11 m/s to 18 m/s is utilized, Fig. 4.1(a). As shown in Fig. 4.1(b), the speed of the rotor follows the trend of the wind speed until the machine reaches the rated power and the pitch control starts to work increasing the pitch angle and extracting energy from the wind in order to avoid machine damage, Fig. 4.1(c).

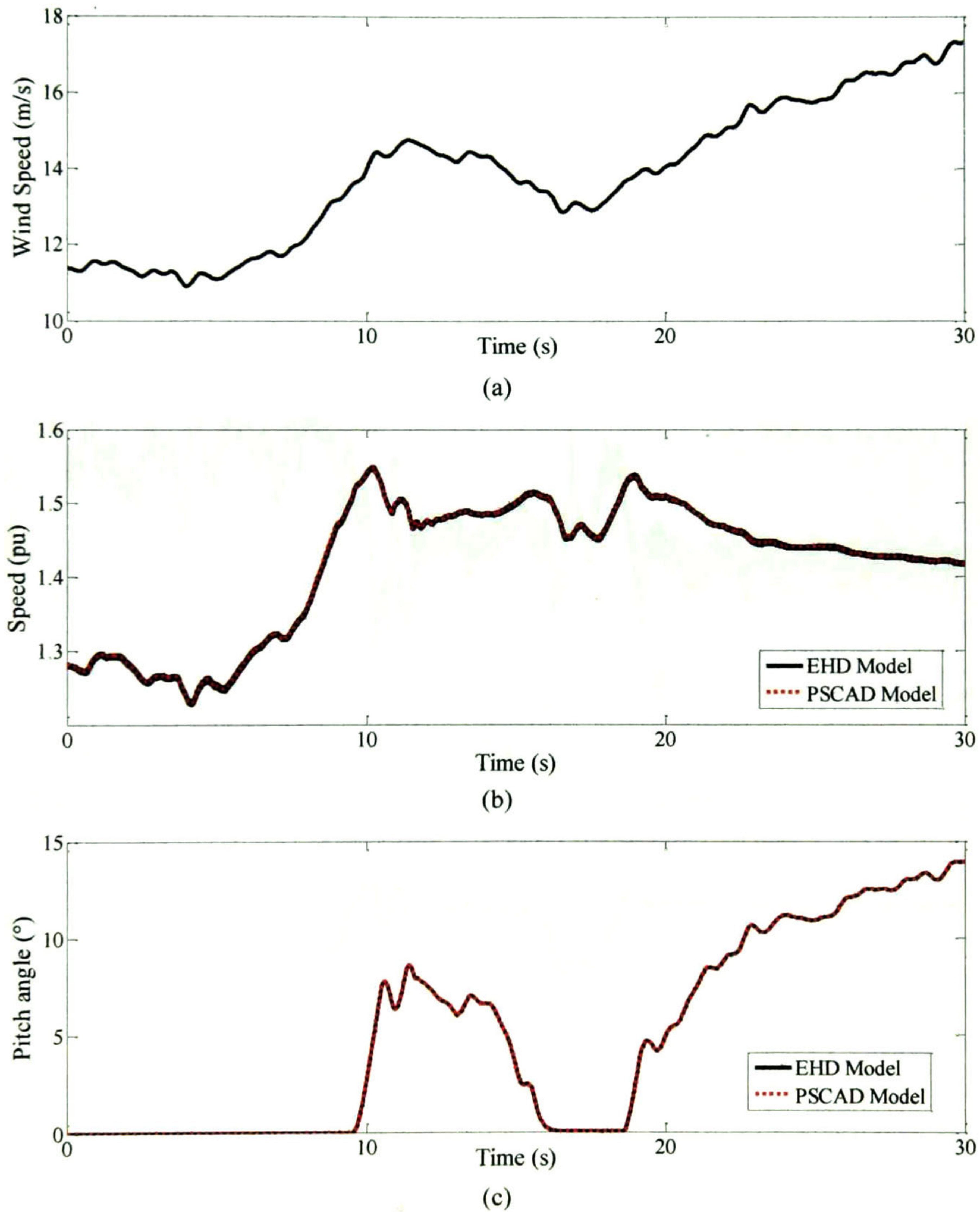


Fig. 4.1. Simulation results a) Wind speed b) Rotor speed c) Pitch angle.

Fig. 4.2(a) presents the turbine mechanical torque whereas Fig. 4.2(b) shows the electromagnetic torque which is set via the MPPT algorithm through the RSC. As shown in Fig. 4.2(c), the power is exceeded when the machine accelerates due to an increasing wind speed and the low speed response of the pitch control. When the pitch control is activated, Fig. 4.1(c), the exceeded power returns to zero.

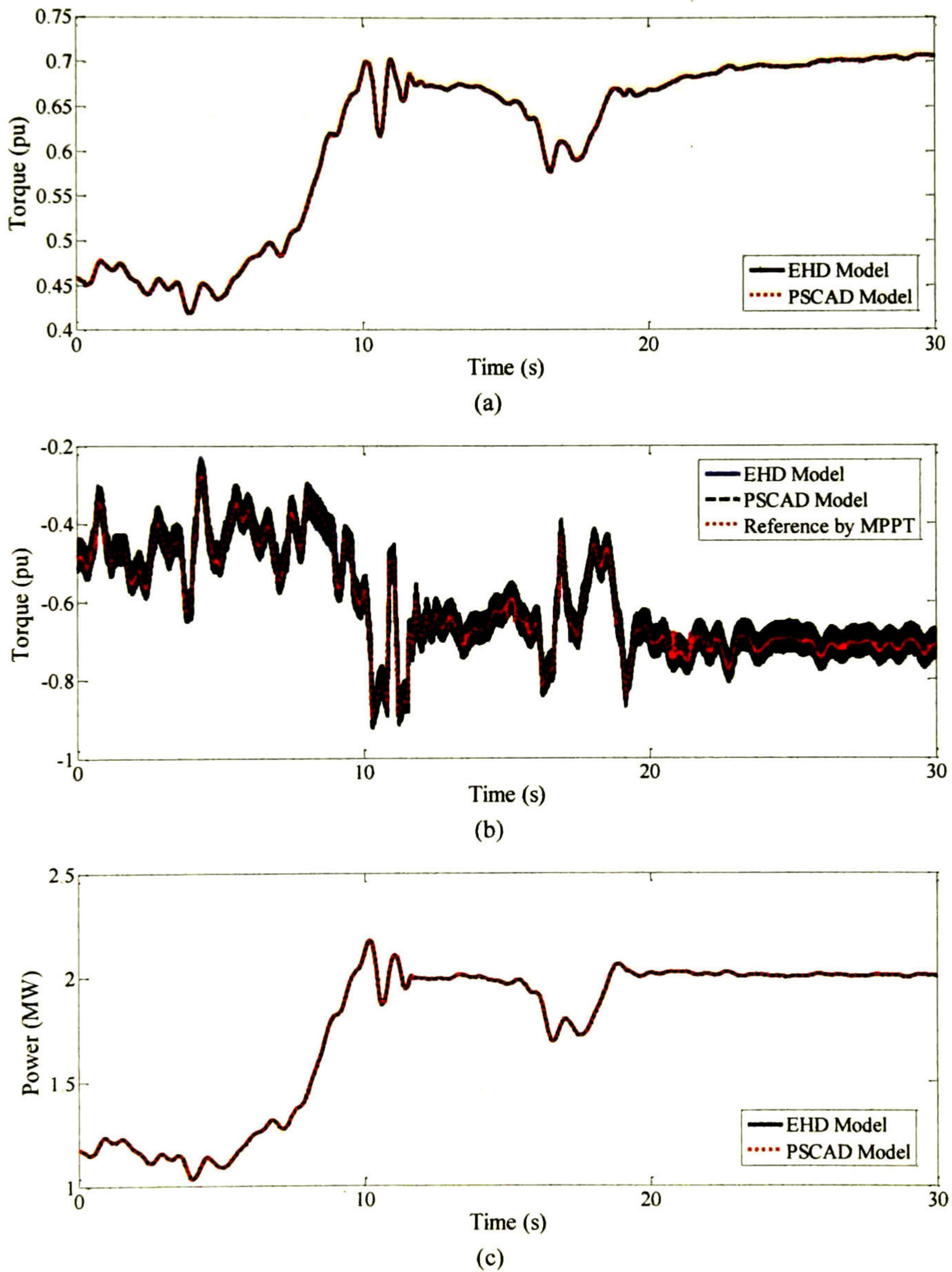


Fig. 4.2. Simulation results a) Turbine mechanical torque b) Electromagnetic torque c) Mechanical power from the turbine.

Fig. 4.3(a) presents the stator current and their corresponding harmonic evolution is presented in Fig. 4.3(b) and Fig. 4.3(c). As expected, the harmonic content in currents is given by the switching function spectrum in the BTB converter, Fig. 3.14.

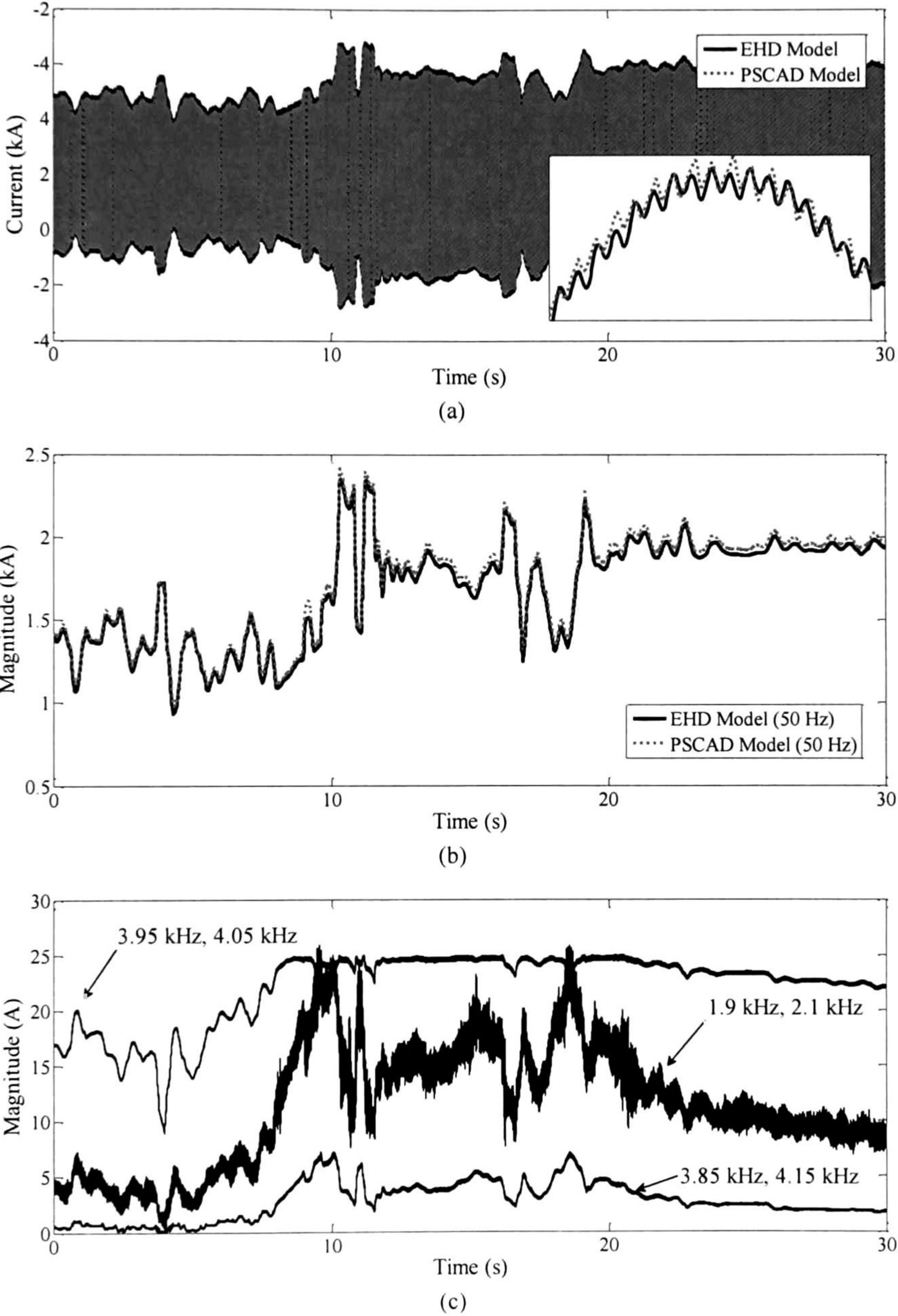


Fig. 4.3. Simulation results a) Stator current b) Stator current at fundamental frequency c) “High-impact” harmonics evolution in stator currents.

Fig. 4.4(a) shows the rotor current and their corresponding harmonic evolution is presented in Fig. 4.4(b) and Fig. 4.4(c). Also, the harmonic content in currents is given by the switching function spectrum in the BTB converter, Fig. 3.14.

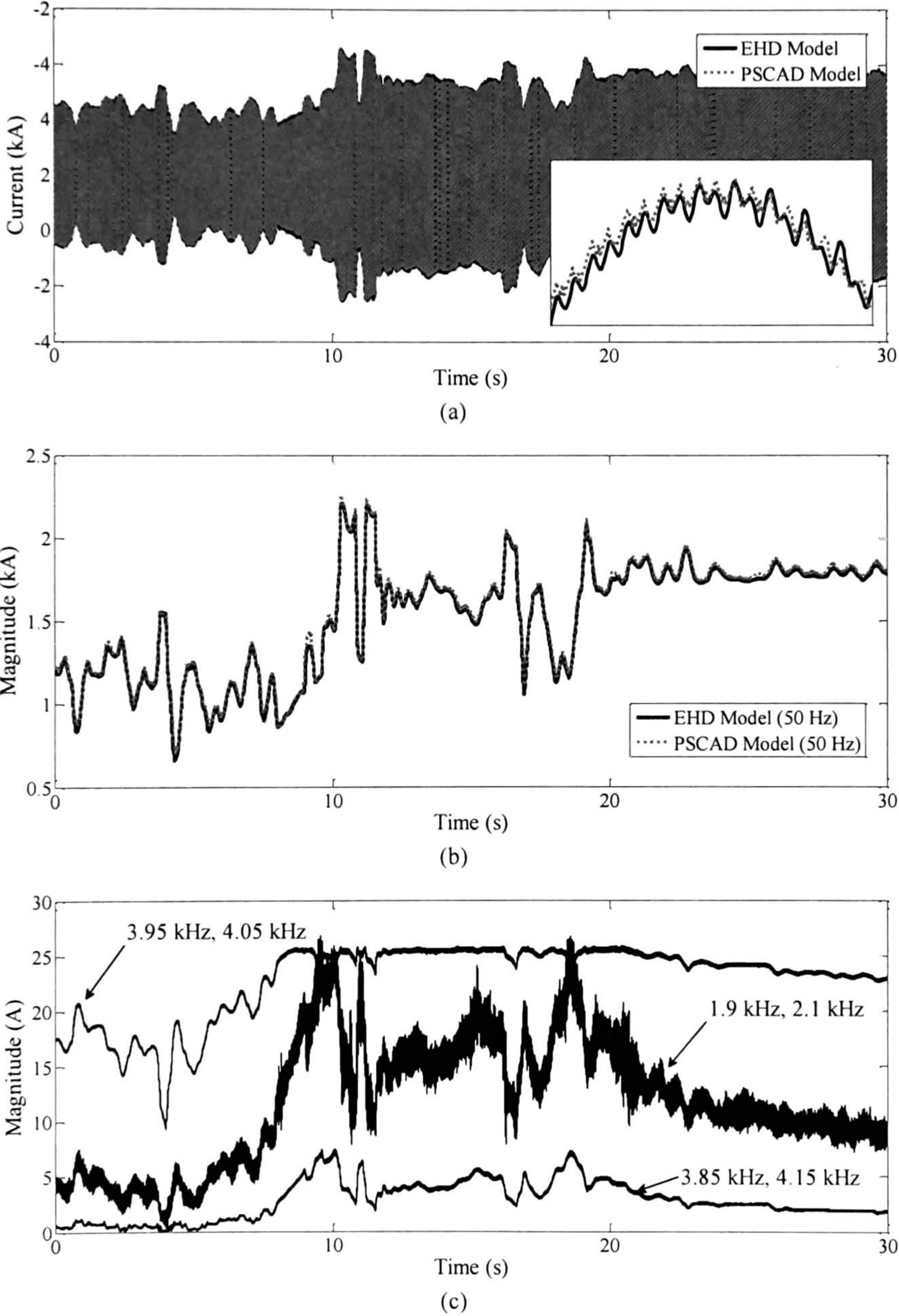


Fig. 4.4. Simulation results a) Rotor current (referred to stator) b) Rotor current at fundamental frequency (referred to stator) c) "High-impact" harmonics evolution in rotor currents (referred to stator).

Depending on the grid configuration, wind speed, and control scheme applied to the system, different power quality problems may arise, e.g., resonance effects, flickering, harmonic distortion, etc. Therefore, it is necessary to address power quality indices. For example, Fig. 4.3(c) and Fig. 4.4(c) show the harmonic evolution in currents which can be utilized to calculate the total harmonic distortion (THD) in both stator and rotor currents, Fig. 4.5, aimed to power quality assessment.

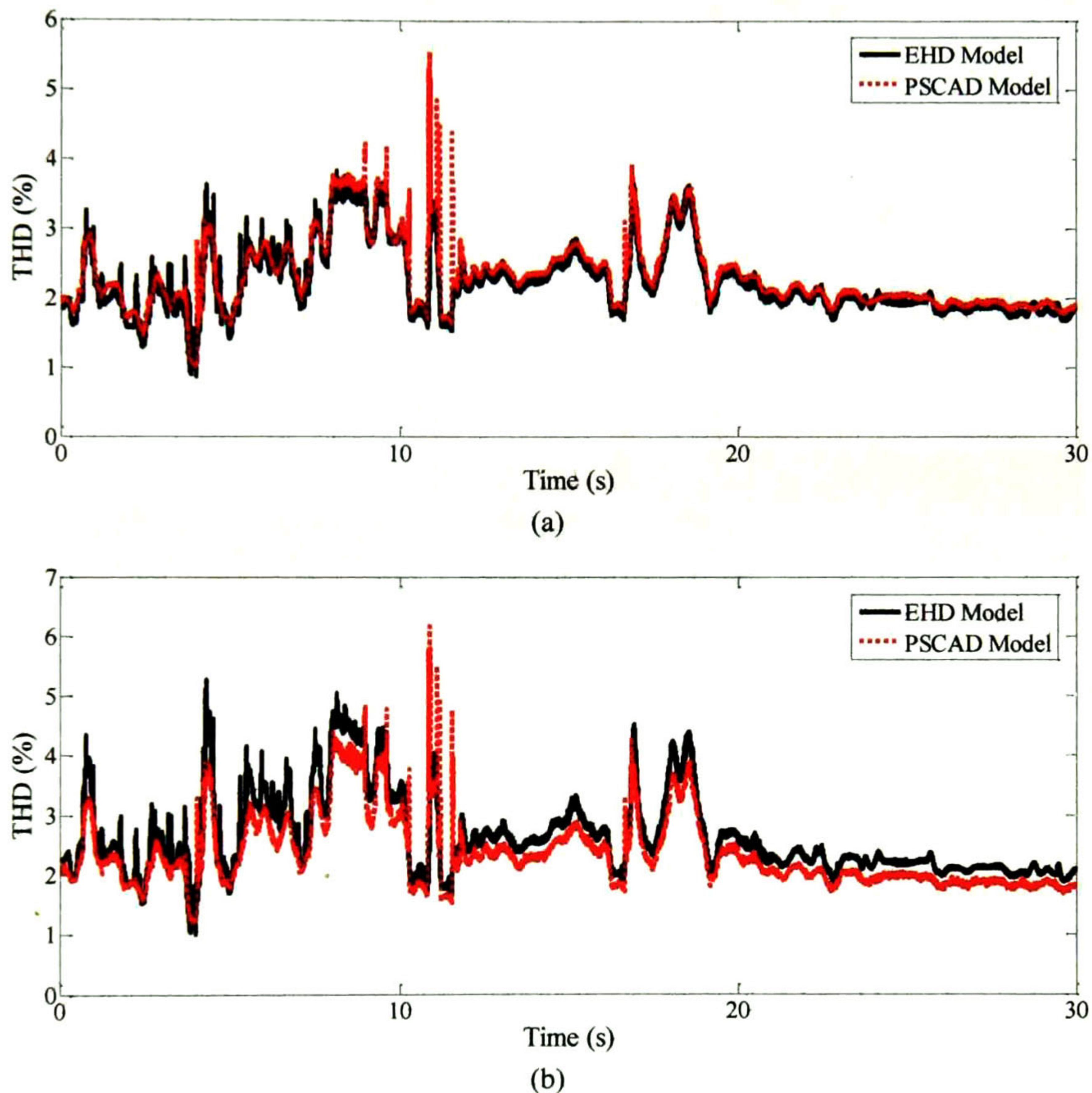


Fig. 4.5. Simulation results a) THD in stator current b) THD in rotor current (referred to stator).

The proposed model is expressed in motor convention; therefore, negative sign in active or reactive powers, Fig. 4.6, means that the machine delivers energy to the grid.

The results in Fig. 4.1 to Fig. 4.6 show a very good agreement between the proposed model and the PSCAD/EMTDC results. Minor differences can be observed in Fig. 4.1 to Fig. 4.6, mainly in high-frequency, which can be attributed to the distinct numerical implementations of firing schemes.

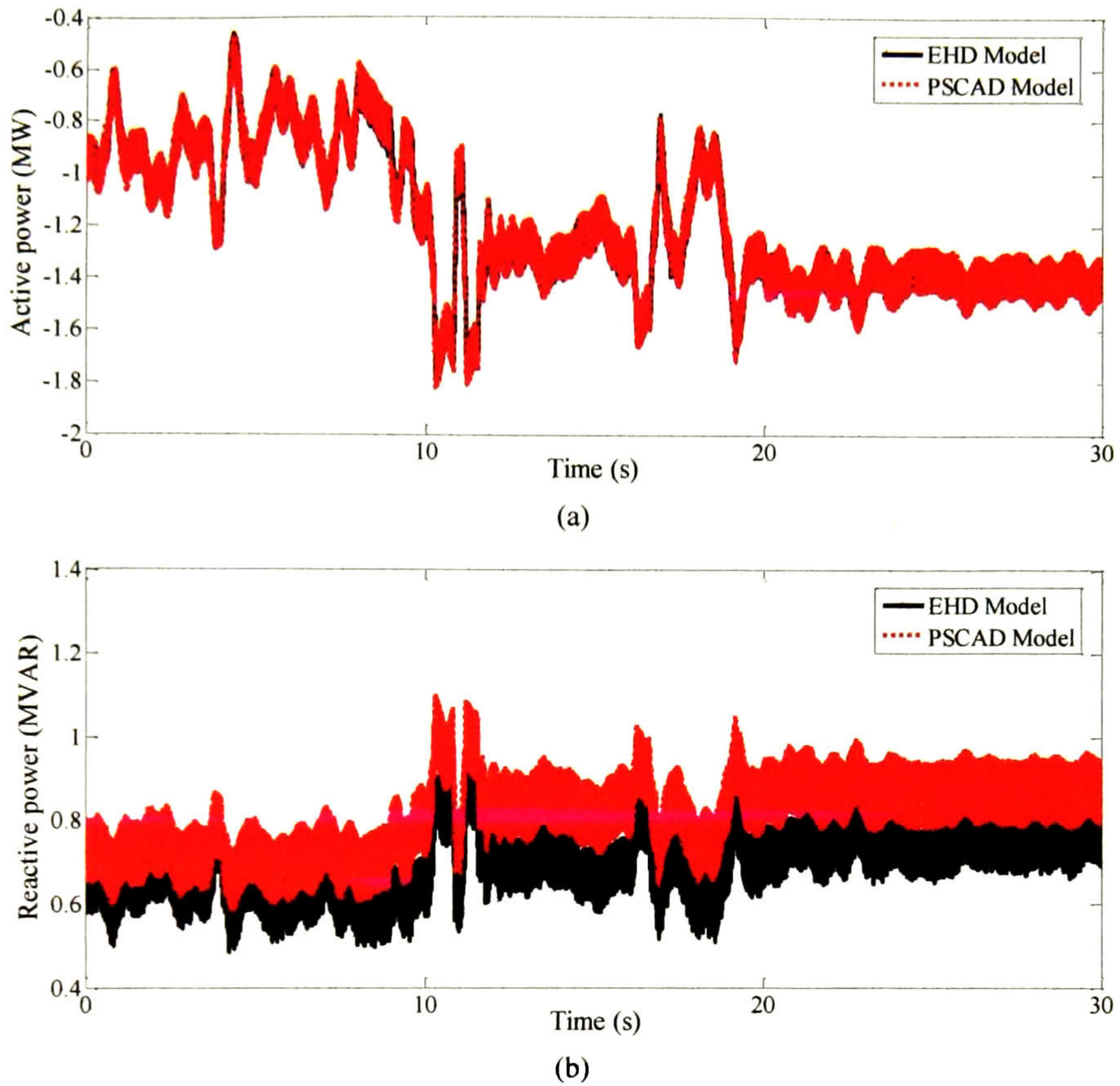


Fig. 4.6. Simulation results a) Active power from the stator b) Reactive power from the stator.

Table 4.2 indicates the simulation data used for this case study, including the CPU times by both the proposed EHD model and the PSCAD/EMTDC simulation. A larger simulation time-step can be used in the proposed model compared to PSCAD/EMTDC while keeping accuracy. Table 4.2 also shows that the CPU times by both models are almost the same. However, the proposed model has been programmed in MatLab's platform, leading to reduced time if programmed in the same platform as PSCAD/EMTDC, i.e., Fortran.

Table 4.2. Simulation data of the case study.

	EHD model (MatLab®)	PSCAD/EMTDC
Simulation time frame	30 s	
Δt (μs)	200	1
CPU time (s)	4906.89	4173.05
Harmonics (h)	1-5, 37-43, 77-83	-
Switching frequency	2 kHz	
Fundamental frequency	50 Hz	

4.3 Conclusions

The proposed WTG EHD model has been evaluated via a case study considering an arbitrary wind-speed range. The obtained results have been compared with the PSCAD software tool showing a very good agreement.

As expected, PSCAD/EMTDC requires a small time-step to achieve a better agreement with the proposed model. This also impacts the CPU time by PSCAD/EMTDC, noting that if the EHD model was programmed in a similar platform (Fortran), its CPU time would be significantly reduced.

A main feature of the proposed model is that it can include any number of harmonics; however, the more harmonics included the larger the state-space EHD system becomes. An efficient heuristic remedy was proposed, which consists on accounting for “high-impact” harmonics only. Moreover, power quality indices can be readily available from the EHD solution.

5 CONCLUSIONS

5.1 Conclusions

The model of a DFIG-based WTG in the EHD aimed to harmonic dynamics analysis has been presented. The proposed model is implemented in MatLab® and validated via a case study. The obtained results have been compared and validated with the PSCAD/EMTDC simulation software tool, showing a very good agreement.

A remarkable characteristic is that the integration time-step of the EHD model can be chosen larger than the one used in the PSCAD/EMTDC simulation; thus, potentially resulting in a faster simulation by the former when programmed in the same platform.

Although the proposed WTG model is in the EHD, any type of control scheme can be applied due to the readily conversion of EHD quantities into TD quantities; besides, any switching function in the TD can easily be converted into the EHD.

A main feature of the proposed model is the insertion of harmonics in mechanical systems, where vibrations can be attributed and expressed in terms of harmonics, produced by electrical variables transmitted via electromechanical systems.

Finally, a major feature of the proposed EHD model is the availability of the instantaneous time-variation of harmonics, which permits to assess power quality in the WTG system and also to evaluate the control scheme performance. On the contrary, the PSCAD/EMTDC requires a post-processing procedure to obtain harmonic frequencies, i.e., using a FFT algorithm, where signals are first sampled and then decomposed into harmonic components, incurring in well-known errors.

5.2 Future work

Some aspects of the proposed WTG EHD model which can be improved are the following:

- a) Implement a frequency control support aimed to the improvement of the WTG control scheme.
- b) Power quality enhancement via space-vector modulation (SVM) and/or multilevel VSC topologies.
- c) Analyze alternative control strategies to improve the WTG performance.
- d) Implement a detailed model of the transformer into the AC grid model.
- e) Introduce EHD WTG models in distributed generation systems.

5.3 Publications

- [1] U. Vargas and A. Ramirez, "Extended harmonic domain model of a wind turbine generator for harmonic dynamics analysis," submitted for publication. *IEEE Trans. Power Del.*, paper TPWRD-00723-2015.
- [2] U. Vargas and A. Ramirez, "Harmonic domain model of a wind turbine generator for steady-state analysis," *accepted in the 2015 North American Power Symposium (NAPS2015)*, paper NAPS 1130.

REFERENCES

- [1] M. Stiebler, *Wind Energy Systems for Electric Power Generation*, Springer Science & Business Media, Germany, 2008.
- [2] S. M. Mueen, *Wind Power*, Intech, Croatia, 2010.
- [3] W. Tong, *Wind Power Generation and Wind Turbine Design*, WIT Press, UK, 2010.
- [4] A. Khaligh and O. C. Onar, *Energy Harvesting: Solar, Wind and Ocean Energy Conversion Systems*, CRC Press, US, 2010.
- [5] F. D. Bianchi, H. De Battista, and R. J. Mantz, *Wind Turbine Control Systems: Principles, Modeling and Gain Scheduling Design*, Springer Science & Business Media, Germany, 2007.
- [6] *IEA Wind: 2013 Annual Report*, IEA Wind, 2014.
- [7] IEA, [Online], Available: <https://www.ieawind.org/countries/mexico.html>, June 2015.
- [8] Enercon, [Online], Available: <http://www.enercon.de>, Sept. 2014.
- [9] Gamesa, [Online], Available: <http://www.gamesacorp.com>, Sept. 2014.
- [10] *Wind Energy--The Facts*, European Wind Energy Association, 2009.
- [11] G. Abad, J. López, M. Rodríguez, L. Marroyo, and G. Iwanski, *Doubly Fed Induction Machine: Modeling and Control for Wind Energy Generation*, John Wiley & Sons Inc., USA, 2011.
- [12] T. Ackermann, *Wind Power in Power Systems*, John Wiley & Sons, England, 2005.
- [13] J. Ekanayake, L. Holdsworth, X. Wu, and N. Jenkins, "Dynamic modeling of doubly fed induction generator wind turbines," *IEEE Trans. Power Syst.*, vol. 18, no. 2, pp. 803-809, May 2003.
- [14] Y. Ren-jie, L. hui, C. Zhe, and G. Qiang, "Comparison of transient behaviors of wind turbines with DFIG considering the shaft flexible models," *Proc. of the International Conference on Electrical Machines and Systems (ICEMS)*, pp. 2585-2590, Oct. 2008.
- [15] M. de Prada, A. Super, and O. Gomis-Bellmunt, "Modeling and control of a pitch-controlled variable-speed wind turbine driven by a DFIG with frequency control support in PSS/E," *Proc. of the IEEE Power Electronics and Machines in Wind Applicat. (PEMWA)*, pp. 1-8, July 2012.
- [16] L. Yazhou, A. Mullane, G. Lightbody, and R. Yacamini, "Modeling of the wind turbine with a doubly fed induction generator for grid integration studies," *IEEE Trans. Energy Convers.*, vol. 21, no. 1, pp. 257-264, March 2006.
- [17] E. Rezaei, A. Tabesh, and M. Ebrahimi, "Dynamic model and control of DFIG wind energy systems based on power transfer matrix," *IEEE Trans. Power Del.*, vol. 27, pp. 1485-1493, July 2012.

- [18] T. Lei, M. Ozakturk, and M. Barnes, "Modelling and analysis of DFIG wind turbine system in PSCAD/EMTDC," *Proc. of the 6th IET International Conference on Power Electronics, Machines and Drives (PEMD)*, pp. 27-29, Bristol, UK, March 2012.
- [19] H. J. Su, H. Y. Huang, and G. W. Chang, "Power quality assessment of wind turbines by Matlab/Simulink," *Proc. of the Asia-Pacific Power and Energy Eng. Conference (APPEEC)*, Chengdu, China, March 2010.
- [20] J. Jesus Rico, M. Madrigal, and E. Acha, "Dynamic harmonic evolution using the extended harmonic domain," *IEEE Trans. Power Del.*, vol. 18, no. 2, pp. 587-594, April 2003.
- [21] Manitoba HVDC Research Centre Inc. Winnipeg, MB, Canada, PSCAD v.4.2.1.
- [22] E. Acha and M. Madrigal, *Power Systems Harmonics*, John Wiley & Sons Inc., US, 2001.
- [23] F. De la Rosa, *Harmonics and Power Systems*, CRC press, US, 2006.
- [24] A. Moreno, *Power Quality: Mitigation Technologies in a Distributed Environment*, Springer Science & Business Media, England, 2007.
- [25] G. T. Heydt, P. S. Fjeld, C. C. Liu, D. Pierce, L. Tu, and G. Hensley, "Applications of the windowed FFT to electric power quality assessment," *IEEE Trans. Power Del.*, vol. 14, no. 4, pp. 1411-1416, Oct. 1999.
- [26] J. Benavent, A. Abellán, and E. Figueres, *Electrónica de Potencia: Teoría y Aplicaciones*, Valencia: Alfaomega Marcombo, 2000.
- [27] B. Gustavsen, "Computer Code for Rational Approximation of Frequency Dependent Admittance Matrices," *IEEE Trans. Power Del.*, vol. 17, no. 4, pp. 1093-1098, Oct. 2002.
- [28] B. Gustavsen and A. Semlyen, "Rational approximation of frequency domain responses by vector fitting," *IEEE Trans. Power Del.*, vol. 14, no. 3, pp. 1052-1061, July 1999.
- [29] B. Gustavsen, "Improving the pole relocating properties of vector fitting," *IEEE Trans. Power Del.*, vol. 21, no. 3, pp. 1587-1592, July 2006.
- [30] D. Deschrijver, M. Mrozowski, T. Dhaene, and D. De Zutter, "Macromodeling of Multiport Systems Using a Fast Implementation of the Vector Fitting Method," *Proc. of the IEEE Microwave and Wireless Components Lett.*, vol. 18, no. 6, pp. 383-385, June 2008.

APPENDIX

Reference frames

Reference frame transformations are a commonly extended tool, traditionally applied in AC machines to represent flux, voltage, and current magnitudes in a simpler way than using the classic three-phase *abc*-representation [11].

The three more common reference frames are [11]:

- The stator reference frame ($\alpha\beta$). Aligned with the stator, the rotating speed of the frame is zero (stationary), and the space vector referred to it rotates at the synchronous speed ω_s .

$$\vec{x}^s = x_\alpha + jx_\beta.$$

- The rotor reference frame (DQ). Aligned with the rotor, the rotating speed of the frame is the rotational speed of the rotor ω_m , and the space vector referred to it rotates at the slip speed ω_r .

$$\vec{x}^r = x_D + jx_Q,$$

where:

$$\omega_r = \omega_s - \omega_m.$$

- The synchronous reference frame (dq). The rotating speed of the frame is the synchronous speed ω_s , and the space vector referred to it does not rotate.

$$\vec{x}^a = x_d + jx_q.$$

Transformations to different reference frames

For developing the dynamic model of the DFIG in $\alpha\beta$ -coordinates, the corresponding relations between the aforementioned reference frames are defined next.

- Transformation from *abc*- to $\alpha\beta$ -coordinates.

$$\vec{X}^s = \begin{bmatrix} X_\alpha \\ X_\beta \end{bmatrix}^s = T_{\alpha\beta} \begin{bmatrix} X_a \\ X_b \\ X_c \end{bmatrix}^s$$

where $T_{\alpha\beta}$ is defined in the HD by

$$T_{\alpha\beta} = \frac{2}{3} \begin{bmatrix} I & -\frac{1}{2}I & -\frac{1}{2}I \\ 0 & \frac{\sqrt{3}}{2}I & -\frac{\sqrt{3}}{2}I \end{bmatrix}, \quad T_{\alpha\beta}^{-1} = \begin{bmatrix} I & 0 \\ -\frac{1}{2}I & \frac{\sqrt{3}}{2}I \\ -\frac{1}{2}I & -\frac{\sqrt{3}}{2}I \end{bmatrix}.$$

- Transformation from abc - to DQ -coordinates.

$$\bar{X}^r = \begin{bmatrix} X_D \\ X_Q \end{bmatrix}^r = T_{DQ} \begin{bmatrix} X_a \\ X_b \\ X_c \end{bmatrix}^r$$

where:

$$T_{DQ} = T_{\alpha\beta}.$$

- Transformation from $\alpha\beta$ - to DQ -coordinates.

$$\bar{x}^s = e^{j\theta_m} \bar{x}^r$$

$$\bar{X}^s = \begin{bmatrix} X_\alpha \\ X_\beta \end{bmatrix}^s = M \begin{bmatrix} X_D \\ X_Q \end{bmatrix}^r$$

where θ_m represents the angular displacement of the rotor, and M is defined in the HD by

$$M = \begin{bmatrix} I \cos \theta_m & -I \sin \theta_m \\ I \sin \theta_m & I \cos \theta_m \end{bmatrix}.$$



CENTRO DE INVESTIGACIÓN Y DE ESTUDIOS AVANZADOS DEL I.P.N. UNIDAD GUADALAJARA

El Jurado designado por la Unidad Guadalajara del Centro de Investigación y de Estudios Avanzados del Instituto Politécnico Nacional aprobó la tesis

"Modelado del Generador Eólico con Máquina de Inducción
Doblemente Alimentada en el Dominio Armónico Extendido"

"Extended Harmonic Domain Modeling of a Wind Turbine with
Doubly Fed Induction Generator"

del (la) C.

Uriel VARGAS GAZCÓN

el día 21 de Agosto de 2015.

Dr. José Manuel Cañedo Castañeda
Investigador CINVESTAV 3C
CINVESTAV Unidad Guadalajara

Dr. Juan Manuel Ramírez Arredondo
Investigador CINVESTAV 3C
CINVESTAV Unidad Guadalajara

Dr. Amner Israel Ramírez Vázquez
Investigador CINVESTAV 3C
CINVESTAV Unidad Guadalajara



CINVESTAV - IPN
Biblioteca Central



SSIT0013367